

Copyright  
by  
Jordan Gilles Attia Mimoun  
2010

**The Thesis Committee for Jordan Gilles Attia Mimoun  
certifies that this is the approved version of the following thesis:**

**Quantitative Interpretation of Pulsed Neutron Capture Logs:  
Fast Numerical Simulation and Inversion in Thinly-Bedded Formations**

**APPROVED BY  
SUPERVISING COMMITTEE:**

---

Carlos Torres-Verdín, Supervisor

---

William E. Preeg, Reader

**Quantitative Interpretation of Pulsed Neutron Capture Logs:  
Fast Numerical Simulation and Inversion in Thinly-Bedded Formations**

**by**

**Jordan Gilles Attia Mimoun, BSE**

**Thesis**

Presented to the Faculty of the Graduate School of

The University of Texas at Austin

in Partial Fulfillment

of the Requirements

for the Degree of

**Master of Science in Engineering**

The University of Texas at Austin

August 2010

## **Dedication**

To Gérard, Monica, Pierre, Simone, and David.

To Gilles, Hélène, Marion, Alexis, and Julien.

To Anna.

## **Acknowledgments**

I owe my most sincere gratitude to my supervisor, Dr. Carlos Torres-Verdín, whose continuous support and exceptional guidance throughout these two years helped to make formation evaluation challenging and exciting. It was a real pleasure and chance to work and study by his side. I have considerably benefitted from his great depth of thinking. I was also very fortunate to have Dr. William E. Preeg as my co-supervisor. His prominent knowledge of pulsed neutron capture tools was insightful and helpful. It was an honor to work under the supervision and co-supervision of Drs. Verdín and Preeg. They provided encouragement, inspiration, sound advice, enthusiasm and a myriad of good ideas.

The work reported in this thesis was made possible thanks to the funding of The University of Texas at Austin's Research Consortium on Formation Evaluation, jointly sponsored by Anadarko, Aramco, Baker Hughes, BG, BHP Billiton, BP, ConocoPhillips, Chevron, ENI, ExxonMobil, Halliburton, Hess, Marathon, Mexican Institute for Petroleum, Nexen, Pathfinder, Petrobras, Repsol-YPF, RWE, Schlumberger, Statoil, TOTAL, and Weatherford.

Special thanks to ConocoPhillips (namely, Gary Simpson and Dr. Jesús Salazar) as well as Schlumberger for providing field data. Special thanks to Dr. Loren Roberts from Baker Hughes for his invitation to their nuclear group's seminar; their suggestions and comments were highly appreciated.

I would like to thank the ExxonMobil Exploration Company for the rewarding internship with their Formation Evaluation group during summer 2009. In addition to

expanding my knowledge, this internship assisted my decision to join Exxon upon graduation.

A note of gratitude to my friend Olabode Ijase for his help and patience. Special thanks to Zoya Heidari, Ankur Gandhi and Kanay Jerath, my colleagues and friends from Office 5.180, where we spent long hours working on inversion, radiation transport, and thermodynamics, to name but a few. I would also like to thank Alberto Mendoza, Renzo Angeles, Jorge Sanchez, Malek Lemkecher, Ali Moinfar, Amir Reza-Rahmani, Robert Mallan, Hamid Hadibeik, Vahid Shabro, Chicheng Xu, Ben Voss, Rohollah Pour, Tatyana Torskaya, Amir Frooqnia, Philippe Marouby, Andy Popielski, Oyin Ajayi and Edwin Ortega.

Reynaldo Casanova, Cheryl Kruzic, Roger Terzian, Tim Guinn, Jin Lee, Frankie Hart, and Erin Gandy deserve special thanks for their administrative support, making the usually cumbersome paperwork so much easier and smoother.

Sylviane Wignacourt deserves a special mention. She triggered the idea of completing my engineering degree from École Centrale de Lille abroad, at the University of Texas. I am infinitely indebted to her for this experience of a lifetime. Not only have my graduate studies made me feel and think like an engineer, but I am sure there is no better place to be but in Texas.

Last but not least, I would like to thank my family and friends for their support. My parents Gérard and Monica, my grandparents Pierre and Simone, my brother David, my uncle and aunt Gilles and Hélène, my cousins Marion, Alexis, and Julien. My girlfriend Anna. My friends Audrey, Amélie, Maëlle, Frédéric, Nicolas, Danny, Philippe, Lionel, Antoine, Luc, Joe, Laurène, Claire, Clément, Laure, and Charlotte. My host mom

Adrienne. Whether they gave birth to me, raised me, or taught me how to walk, run, read, write, laugh, and live; whether they were next to me during the merriest or the toughest episodes of my life; whether they gave me their unflagging love, their thrilling companionship, their unfailing friendship, their spiritual mentorship, they all have contributed to making me a better person. Thanks y'all. Merci à vous tous.

They say that what starts here changes the world. They are right.

August 2010

## **Abstract**

# **Quantitative Interpretation of Pulsed Neutron Capture Logs: Fast Numerical Simulation and Inversion in Thinly-Bedded Formations**

Jordan Gilles Attia Mimoun, MSE

The University of Texas at Austin, 2010

Supervisor: Carlos Torres-Verdín

Pulsed neutron capture (PNC) logs are commonly used for formation evaluation behind casing and to assess time-lapse variations of hydrocarbon pore volume. Because conventional interpretation methods for sigma logs assume homogeneous formations, errors may arise, especially in thinly-bedded formations, when appraising petrophysical properties of hydrocarbon-bearing beds. There exist no quantitative interpretation methods to account for shoulder-bed effects on sigma logs acquired in sand-shale laminated reservoirs. Because of diffusion effects between dissimilar beds, sigma logs acquired in such formations do not obey mixing laws between the sigma responses of pure-sand and pure-shale end members of the sedimentary sequence.



We introduce a new numerical method to simulate rapidly and accurately PNC logs. The method makes use of late-time, thermal-neutron flux sensitivity functions (FSFs) to describe the contribution of multi-layer formations toward the measured capture cross section. It includes a correction procedure based on 1D neutron diffusion theory that adapts the transport-equation-derived, base-case FSF of a homogeneous formation to simulate the response of vertically heterogeneous formations. Benchmarking exercises indicate that our simulation method yields average differences smaller than 2 c.u. within seconds of CPU time with respect to PNC logs simulated with rigorous Monte Carlo methods for a wide range of geometrical, petrophysical, and fluid properties.

We develop an inversion method to reduce shoulder-bed effects on pulsed neutron capture (PNC) logs in the estimation of layer-by-layer capture cross sections,  $\Sigma$ . The method is based on the previously developed rapid approximation of PNC logs. Tests performed on synthetic examples that include a variety of lithology, saturating-fluid, and bed-thickness configurations confirm the efficiency, reliability, and stability of the inversion procedure. Inversion consistently improves the vertical resolution and  $\Sigma$  definition of PNC logs across beds thinner than 45 cm. Our fast, iterative algorithm inverts sigma logs in seconds of CPU time, and is therefore suitable for joint petrophysical interpretation with other open- and cased-hole logs.

## Table of Contents

List of Tables .....	xii
List of Figures .....	xv
Chapter 1: Introduction .....	1
1.1 Background .....	1
1.2 Problem Statement .....	2
1.3 Outline of the Thesis .....	4
Chapter 2: Monte Carlo-Simulated Measurements .....	5
2.1 Tool Configuration .....	5
2.2 Monte Carlo Methods .....	6
2.3 Procedure .....	7
2.4 Variance Reduction Techniques .....	8
Chapter 3: Limitations of $\Sigma$ Mixing Laws .....	9
3.1 Linear Mixing Laws .....	9
3.2 Stieber Mixing Law .....	9
3.3 PNC Measurements in Heterogeneous Formations .....	10
Chapter 4: Formulation of the Problem .....	13
Chapter 5: Dependence of FSFs on Formation Properties .....	15
5.1 Homogeneous Formations .....	15
5.2 Impact of Heterogeneities .....	20
5.3 Radial Length of Investigation .....	22
Chapter 6: Fast Numerical Simulation of PNC logs .....	24
6.1 Method .....	24
6.2 Transport of Gamma Rays .....	25
6.3 Synthetic Cases .....	26
6.3.1 Synthetic Case No. 1: Turbidite Formation .....	26
6.3.2 Synthetic Case No. 2: Complex Multi-Layer Formation .....	28

Chapter 7: Inversion in Thinly-Bedded Formations .....	33
7.1 Background and Objectives .....	33
7.2 Formulation.....	35
7.2.1 Petrophysical Framework .....	35
7.2.2 Inversion of PNC Logs .....	36
7.2.3 Iterative Inversion Algorithm .....	37
7.3 Synthetic Examples.....	40
7.3.1 Synthetic Case No. 3 .....	40
7.3.2 Synthetic Case No. 4.....	45
7.4 Field Examples .....	51
7.4.1 Field Case No. 1.....	51
7.4.2 Field Case No. 2.....	55
Chapter 8: Conclusions and Recommendations .....	58
8.1 Conclusions.....	58
8.1.1 Fast Numerical Simulation of PNC Logs .....	58
8.1.2 Inversion in Thinly-Bedded Formations.....	60
8.2 Recommendations.....	62
Appendix A: FSF-Correction Procedure Based on 1D Diffusion Theory .....	64
A.1 Assumptions.....	64
A.2 Formulation.....	65
A.3 Results.....	67
Nomenclature and Acronyms .....	70
References.....	73
Vita .....	78

## List of Tables

<b>Table 2.1:</b>	Formation thermal decay time at the near detector calculated with MCNP simulations of the Longhorn PNC tool $\tau_{sim}$ , compared against experimental results $\tau_{exp}$ , for several values of salt concentration of formation water ( $C_{wF}$ ) and borehole fluid ( $C_{wBH}$ ). The assumed formation is a homogeneous, 30.4%-porosity sandstone, with 25.4-cm-diameter borehole, 17.8-cm-diameter casing. $\Delta\tau$ is the relative error between $\tau_{exp}$ and $\tau_{sim}$ ; $\Delta\Sigma$ is the corresponding absolute error on capture cross section .....6
<b>Table 3.1:</b>	Formation capture cross section calculated with MCNP simulations of the Longhorn PNC tool $\Sigma_{MCNP}$ , compared against estimations from the linear mixing law, $\Sigma_{Linear}$ , as well as from the nonlinear Stieber model, $\Sigma_{Stieber}$ . $\Delta\Sigma$ is the error between $\Sigma_{MCNP}$ and each of these estimations. .... 11
<b>Table 5.1:</b>	Summary of the assumed lithology and saturating fluid, porosity $\phi$ , bulk density $\rho_b$ , hydrogen index $HI$ , slowing-down length $L_s$ , and intrinsic capture cross section $\Sigma_{int}$ , for the 3 formations whose FSFs are reported in Figure 5.2. SNUPAR (McKeon and Scott, 1989) was used to calculate $L_s$ and $\Sigma_{int}$ . .... 17
<b>Table 5.2:</b>	Summary of the assumed petrophysical properties for the 8 cases whose FSFs are reported in Figure 5.3. The formations consist of a homogeneous sandstone layer, saturated either with fresh water (Formation “A”) or with 200-kppm salt water (Formation “B”). Slowing-down length $L_s$ , diffusion coefficient $D$ , and intrinsic capture cross section $\Sigma_{int}$ were calculated with SNUPAR. .... 17
<b>Table 5.3:</b>	Summary of the assumed petrophysical and borehole geometry properties for the 6 cases whose radial J-factors are reported in Figure 5.5. Borehole salinity of 250 kppm is common to all 6 cases. $\Sigma_{int}$ was calculated with SNUPAR..... 22
<b>Table 6.1:</b>	Summary of the assumed values of total porosity $\phi$ , saturation $S$ , formation water salt concentration $C_{wF}$ , intrinsic capture cross section $\Sigma_{int}$ (from SNUPAR) and expected measured capture cross section $\Sigma_{dif}$ (from MCNP) for the sand and shale components of Synthetic Case No. 1..... 27

<b>Table 6.2:</b>	Summary of the assumed hydrocarbon densities, borehole fluid properties, well geometry and sampling rate for Synthetic Cases No. 1 and 2.....	27
<b>Table 6.3:</b>	Summary for Synthetic Case No. 2 of the assumed lithology, bed thickness $2H$ , non-shale porosity $\phi_s$ , shale porosity $\phi_{sh}$ , volumetric concentration of shale $C_{sh}$ , water saturation $S_w$ , formation water salt concentration $C_{wF}$ , nature of the hydrocarbons HC, slowing-down length $L_s$ (from SNUPAR), intrinsic capture cross section $\Sigma_{int}$ (from SNUPAR), and expected measured capture cross section $\Sigma_{dif}$ (from MCNP simulations of the pure, infinite-extent formation in the presence of the borehole), from top to bottom of the formation..	30
<b>Table 7.1:</b>	Summary of the assumed lithology, bed thickness $2H$ , total porosity $\phi$ , saturation $S$ , formation water salt concentration $C_{wF}$ , and intrinsic capture cross section $\Sigma_{int}$ for Synthetic Case No. 3, from top to bottom of the formation. $\Sigma_{int}$ was determined from SNUPAR.....	42
<b>Table 7.2:</b>	Summary of the assumed hydrocarbon densities, borehole fluid properties, well geometry and sampling rate for Synthetic Cases Nos. 3 and 4. ....	43
<b>Table 7.3:</b>	Final layer-by-layer capture cross sections $\Sigma_{est}$ estimated upon matching the measured log with fast-forward simulations, from top to bottom of the formation, for Synthetic Case No. 3. $\Sigma_{dif}$ is the expected measured capture cross section (from MCNP). $\Delta\Sigma$ is the error (both absolute and relative) between $\Sigma_{est}$ and $\Sigma_{dif}$ . $\delta\Sigma_{95}$ quantifies the uncertainty in the appraisal (95% confidence interval).....	43
<b>Table 7.4:</b>	Summary of the assumed values of total porosity $\phi$ , saturation $S$ , formation water salt concentration $C_{wF}$ , intrinsic capture cross section $\Sigma_{int}$ (from SNUPAR) and expected measured capture cross section $\Sigma_{dif}$ (from MCNP) for the sand and shale components of Synthetic Case No. 4.....	48
<b>Table 7.6:</b>	Summary of the borehole diameter and sampling rate, as well as the assumed formation water and borehole fluid properties for Field Case No. 1.....	52

<b>Table 7.7:</b>	Summary of the assumed lithology, bed thickness $2H$ , porosity $\phi$ , estimated capture cross section $\Sigma_{est}$ , and corresponding 95% confidence interval $\delta\Sigma_{95}$ , from top to bottom of the formation, for Field Case No. 1.....	53
<b>Table 7.8:</b>	Summary of the average formation and fluid properties assumed for Field Case No. 2.....	56
<b>Table A.1:</b>	Thermal decay time $\tau$ for various materials (calculated with SNUPAR). .....	65

## List of Figures

- Figure 3.1:** Case No. 1 (left) consists of a 48.2-c.u. shale layer overlaid by a 14.3-c.u. oil-bearing sand layer. Case No. 2 (right) consists of the same shale layer below a 6.5-c.u. gas-bearing sand layer. Orange-colored lines at 0 and 35 cm describe the positions of source and detector, respectively. ....11
- Figure 5.1:** Thermal-neutron FSF corresponding to PNC measurements acquired with the Longhorn tool in a 25-% porosity sandstone formation saturated with fresh water. The left panel shows the 2D spatial sensitivity of PNC measurements in the formation, and the right panel describes the corresponding 1D plot along the borehole tool, integrated in the radial direction. Orange-colored lines at 0 and 35 cm indicate the positions of source and detector, respectively. For plotting purposes, the FSF was normalized to show variations between 0 and 1. The borehole configuration is: 25.4-cm borehole diameter, 1.78-cm casing and 250-kppm salt water.....16
- Figure 5.2:** Impact of slowing-down length  $L_s$  on the spatial sensitivity of PNC measurements acquired with the Longhorn tool, with source and detectors located as indicated by the orange-colored lines at 0 and 35 cm, respectively. Simulations assume a common borehole configuration for all 3 cases: 25.4-cm borehole diameter, 17.8-cm casing diameter and 250-kppm borehole fluid. Unlike in Figure 5.1, the normalization was done according to equation (4.2). .....18
- Figure 5.3:** Impact of  $\Sigma$  on the spatial sensitivity of PNC measurements acquired with the Longhorn tool in homogeneous formations. Blue and red lines represent the thermal-neutron FSFs for a homogeneous sand layer, either saturated with fresh water or with 250-kppm salt water, respectively. Porosity varies from 5% (top left panel) to 35% (bottom right panel). Orange-colored lines at 0 and 35 cm describe the positions of source and detector, respectively. Simulations assume a common borehole configuration for all 3 cases: 25.4-cm-diameter borehole, 17.8-cm-diameter casing and 250-kppm borehole fluid. Normalization was implemented according to equation (4.2). ....19

<b>Figure 5.4:</b>	Comparison of MCNP-generated thermal-neutron FSFs for the layered formation (solid red line) against the FSF for a homogeneous formation (dashed black line), for Cases Nos. 1 (left panel) and 2 (right panel). Orange-colored lines at 0 and 35 cm indicate the location of source and detector, respectively. Normalization was implemented in agreement with equation (4.2). . . . .	21
<b>Figure 5.5:</b>	Radial J-factors of the FSFs for 6 different cases. Red and blue lines describe the geometric factors for oil-bearing sand and shale formations, respectively. Solid lines identify the case of a 25.4-cm-diameter openhole. Dotted lines describe the case of a 25.4-cm-diameter borehole and 17.8-cm-diameter casing configuration. Dashed lines assume a 30.5-cm-diameter borehole, 24.4-cm-diameter casing. The green line identifies the radial length of investigation in the sense of Sherman and Locke (1975), i.e. the 90% value of the radial J-factor. . . . .	23
<b>Figure 6.1:</b>	Comparison of numerically simulated (solid red line) and measured $\Sigma$ logs (solid green line, calculated with MCNP) for Synthetic Case No. 1. Actual layer-by-layer values are described with the dashed blue line. . . . .	29
<b>Figure 6.2:</b>	Comparison of numerically simulated (solid red line) and measured $\Sigma$ logs (solid green line, calculated with MCNP) for Synthetic Case No. 2. Actual layer-by-layer values are described with the dashed blue line. . . . .	32
<b>Figure 7.1:</b>	Flowchart of the fast-forward and inversion method developed for PNC logs. The agreement (match) between numerical simulations and measurements is ascertained from the increment in model parameters from one iteration to the next, which is verified against a pre-specified threshold. . . . .	39
<b>Figure 7.2:</b>	Comparison of estimated layer-by-layer $\Sigma$ values (dashed red line) and true model values (dashed blue line) for Synthetic Case No. 3. Numerically simulated and measured $\Sigma$ logs are indicated with solid red and green lines, respectively. The inversion was initialized with a parsimonious guess based on the average value of the measured log (dashed green line). Black error bars describe the 95% confidence interval. . . . .	44



<b>Table 7.5:</b>	Final layer-by-layer capture cross sections $\Sigma_{est}$ estimated by the iterative inversion method applied to Synthetic Case No. 4, from top to bottom of the formation. $2H$ is bed thickness. $\Delta\Sigma$ is the error between $\Sigma_{est}$ and $\Sigma_{dif}$ (reported in Table 7.4). $\delta\Sigma_{95}$ quantifies the uncertainty of the appraisal (95% confidence interval). .....	48
<b>Figure 7.3:</b>	Comparison of estimated layer-by-layer $\Sigma$ values (dashed red line) and true model values (dashed blue line) for Synthetic Case No. 4. Numerically and measured $\Sigma$ logs are indicated with solid red and green lines, respectively. The inversion was initialized with a parsimonious guess based on the average value of the measured log (dashed green line). Black error bars describe the 95% confidence interval. ....	49
<b>Figure 7.4:</b>	Impact of bed-boundary perturbation on the estimated layer-by-layer $\Sigma$ values (dashed red line) for Synthetic Case No. 4. The true model is displayed with a dashed blue line. Numerically and measured $\Sigma$ logs are indicated with solid red and green lines, respectively. The inversion was initialized with a parsimonious guess based on the average value of the measured log (dashed green line). Black error bars describe the 95% confidence interval. .	50
<b>Figure 7.5:</b>	Comparison of numerically simulated (solid red line) and measured (solid blue line) PNC logs (right-hand track) for Field Case No. 1. The dashed blue line describes the initial guess, which is the average value of the measurements in this interval. Estimated layer-by-layer sigma values are indicated with dashed red lines, together with black error bars that quantify the 95% confidence interval. The left-hand track displays thermal neutron decay porosity (green) and density porosity (red) logs, respectively. ....	54
<b>Figure 7.6:</b>	Comparison of numerically simulated (solid red line) and measured (solid blue line) PNC logs (track 4) for Field Case No. 2. The dashed blue line describes the initial guess, which is the average value of the measurements in this interval. Estimated layer-by-layer sigma values are indicated with dashed black lines. Track 1 displays the gamma-ray log; track 2 shows the array-induction resistivity logs; track 3 shows the neutron porosity log. ...	57

**Figure A.1:** Comparison of late-time, thermal-neutron FSFs simulated with the diffusion-approximation correction (dashed red line) and MCNP (solid blue line), for formations with similar slowing-down lengths (oil-, water-bearing sand, and shale formations). We initialized the correction procedure using the base-case FSF represented in dashed black line. Orange-colored lines at 0 and 35 cm describe the positions of source and detector, respectively. ....68

**Figure A.2:** Comparison of late-time, thermal-neutron FSFs simulated with the diffusion-approximation correction (dashed red line) and MCNP (solid blue line), for formations with different slowing-down lengths. We initialized the correction procedure using the regular base-case FSF (dashed black line) that is tailored to oil- and water-saturated formations (represented in light and dark green). For the gas-bearing formation (represented in yellow), we made use of a specific gas-formation FSF. Orange-colored lines at 0 and 35 cm describe the positions of source and detector, respectively. ....69

# Chapter 1: Introduction

## 1.1 BACKGROUND

Since the early days of Neutron Lifetime<sup>1</sup> and Thermal Neutron Decay Time<sup>2</sup> (TDT) logging instruments (Youmans et al., 1964; Wahl et al., 1970), PNC tools have become indispensable for cased-hole saturation monitoring.

PNC logs are used to discriminate hydrocarbon- from water-bearing reservoir units because of the sizable difference of thermal-neutron decay rates in saline water and hydrocarbons. The difference in physical behavior stems from the presence of chlorine in water, which is the strongest absorber of neutrons in common subsurface formations. In addition to identifying pay zones among water-saturated layers, PNC measurements are acquired throughout the life of hydrocarbon-producing wells to monitor variations of saturation with time. Time-lapse monitoring is a widely used application of sigma logs in the petroleum industry and has received much attention (Clavier et al., 1971b; Nutt and Watfa, 1989; Kimminau and Plasek, 1992; Cowan and Wright, 1999). The extension of time-lapse logging in waterflooded reservoirs is the estimation of waterflood residual oil saturation via the log-inject-log procedure (Richardson et al., 1973; Reedy, 1984). Also, equipping PNC tools with dual-detector systems improves the detection of gas, reduces

---

<sup>1</sup> Trademark of Lane-Wells Co. (now Baker Hughes).

<sup>2</sup> Trademark of Schlumberger.

borehole environmental effects, and provides the interpreter with an apparent porosity from the ratio of both detectors' counts (Dewan et al., 1973; Serpas et al., 1977).

Despite recent breakthroughs in resistivity measurements behind casing (Bartenhagen et al., 2001), the need remains for resistivity-independent saturation evaluation in both open- and cased-hole logging operations. Low-contrast, low-resistivity pays (Simpson and Menke, 2010) as well as non-Archie formations (e.g. carbonates and shaly sands) may limit the reliance on resistivity measurements, hence the need for an alternative method for saturation appraisal and cross-validation of interpretations. This is why the PNC time-lapse technique is routinely used in hydrocarbon-producing wells: sigma changes can be directly associated with fluid-saturation changes.

## **1.2 PROBLEM STATEMENT**

To date, simulating PNC measurements with rigorous Monte Carlo methods remains the standard method used to quantify PNC tool responses (Butler, 1987). Previous attempts were made to develop interpretation methods based on Monte Carlo simulators, such as described by Peeters et al. (1994). Nevertheless, the large CPU time associated with Monte Carlo techniques renders them impractical to implement inversion methods in either the assessment of complex lithologies or the joint quantitative petrophysical interpretation with other open- or cased-hole borehole measurements.

There also exist finite-difference numerical simulators of PNC measurements based on diffusion theory. Even though the underlying physics is governed by the Boltzmann transport equation, in some instances it may be approximated by neutron diffusion. In that context, it is worth noting that Jennings and Weber (1995) took a remarkable first step toward the fast quantitative interpretation of PNC logs. However, borehole environmental effects may cause significant simulation errors: Hamzah (1996) reported errors on the simulated counts above 30% in the cases of 15.2- and 25.4-cm-diameter boreholes filled with salt water. This is why the departure curves for TDT determined by Locke and Smith (1975) with a diffusion-based numerical simulator were eventually substituted with Monte Carlo-based numerical simulation techniques (Preeg and Scott, 1986).

In similar fashion to Mendoza et al.'s (2010) approach to numerically simulate neutron and density measurements, in this paper we develop a new method for the fast simulation of PNC measurements using Monte Carlo-derived flux sensitivity functions (FSFs). However, unlike neutron and density measurements, PNC measurements can be substantially affected by shoulder beds to the extent that it is not possible to pre-compute such FSFs for all multi-layer cases. Instead, simulations are initialized with base-case FSFs for homogeneous formations, to subsequently account for vertical heterogeneities by adapting the FSFs to the presence of layer boundaries using 1D diffusion theory.

To benchmark our FSF-correction method, we generate synthetic PNC measurements using the Monte Carlo N-Particle<sup>3</sup> (MCNP) code (X-5 Monte Carlo Team, 2003). We also calculate the corresponding multi-layer FSFs with MCNP, which we compare to diffusion-corrected FSFs. The excellent agreement with the calculated  $\Sigma$  for the two methods validates our FSF-correction strategy, thereby enabling the rapid numerical simulation of PNC logs with no further need of Monte Carlo methods.

### **1.3 OUTLINE OF THE THESIS**

Following the introductory chapter, the thesis consists of six additional chapters. Chapter 2 gives details about the generation of PNC measurements with Monte Carlo simulations of the generic PNC tool. Chapter 3 analyses the limitations of mixing laws for  $\Sigma$  in heterogeneous formations. Formulation of the problem is reported in Chapter 4, while Chapter 5 sheds light on the dependence of the FSFs on formation properties.

Chapter 6 develops a new method to rapidly simulation PNC measurements with the use of the previously introduced FSFs.

Chapter 7 implements the rapid simulation of PNC measurements for their inversion in thinly-bedded formations, illustrated by two synthetic examples and three field cases.

Chapter 8 summarizes the general conclusions and future research recommendations stemming from this thesis.

---

<sup>3</sup> Trademark of Los Alamos National Laboratory.

## Chapter 2: Monte Carlo-Simulated Measurements

### 2.1 TOOL CONFIGURATION

Throughout this study, we generate PNC logs using both Monte Carlo simulations and the fast, approximate numerical method described in a subsequent section of this thesis. Monte Carlo-derived synthetic PNC logs will serve as benchmark in the study.

We first invoke a generic Longhorn PNC tool that exhibits the traditional configuration of sigma logging tools. It includes a 14-MeV accelerator source, which emits fast neutrons through both casing and cement into surrounding rock formations. Since the earliest days of PNC logging it has been recognized that detecting neutron-capture gamma rays is preferable to detecting neutrons (Youmans et al., 1964; Mills et al., 1965; Wahl et al., 1970). This is the reason why we equip the Longhorn tool with two scintillation crystals, which are located 35 and 58 cm away from the source, respectively. Owing to its better vertical resolution, henceforth we exclusively focus our attention to the photon counting rate at the short-spaced detector.

The hypothetical 4.30-cm-diameter tool exhibits a measurement response similar to commercial tools. **Table 2.1** reports comparisons against experimental results reported by Preeg and Scott (1986), which indicate less than 1.25% error for the Longhorn PNC tool in terms of MCNP-simulated measurements of formation thermal decay time,  $\tau$ , at the near detector. In terms of  $\Sigma$ , this represents an error below 0.20-c.u.

$C_{wF}$ [kppm]	$C_{wBH}$ [kppm]	$\tau_{sim}$ [ $\mu$ s]	$\tau_{exp}$ [ $\mu$ s]	$\Delta\tau$ [%]	$\Delta\Sigma$ [c.u.]
36.9	0	277.4	274	1.25	-0.20
36.9	36.9	271.4	270	0.53	-0.09
36.9	250	270	270	0.01	0
73.7	0	213.7	214	-0.13	0.03
73.7	73.7	213.8	214	-0.09	0.10
73.7	250	213.3	212	0.61	-0.13

**Table 2.1:** Formation thermal decay time at the near detector calculated with MCNP simulations of the Longhorn PNC tool  $\tau_{sim}$ , compared against experimental results  $\tau_{exp}$ , for several values of salt concentration of formation water ( $C_{wF}$ ) and borehole fluid ( $C_{wBH}$ ). The assumed formation is a homogeneous, 30.4%-porosity sandstone, with 25.4-cm-diameter borehole, 17.8-cm-diameter casing.  $\Delta\tau$  is the relative error between  $\tau_{exp}$  and  $\tau_{sim}$ ;  $\Delta\Sigma$  is the corresponding absolute error on capture cross section

## 2.2 MONTE CARLO METHODS

Because the Boltzmann equation, which describes the transport of neutrons, cannot be solved analytically in a borehole-and-formation geometry (Steinman et al., 1988), we instead resort to numerical solutions. To that end, we use the Monte Carlo code MCNP that reproduces the transport of neutrons and photons, from the emission of fast neutrons and their slowing down through numerous collisions with atomic nuclei, to their capture and subsequent emission of neutron-induced gamma rays that are counted at the detector. Unlike deterministic methods, Monte Carlo methods need no averaging approximations in space, energy or time, and they can easily include arbitrary distributions of material properties. This flexibility makes MCNP a commonly used technique for simulating such borehole nuclear measurements.



### 2.3 PROCEDURE

From MCNP results we obtain gamma-ray counts at the near detector, which are similar to those acquired in practice. Even though some of the recently commercialized PNC tools resort to a dynamic parameterization technique based on a database of laboratory measurements (Plasek et al., 1995), Morris et al. (2005) reported that the traditional signal processing technique based on fitting the data with two exponential decays is reliable to separate borehole and formation responses. Thus, we express the photon counts as a function of time,  $M(t)$ , as

$$M(t) = A_{\text{BH}} \exp\left(-\frac{t}{\tau_{\text{BH}}}\right) + A_{\text{F}} \exp\left(-\frac{t}{\tau_{\text{F}}}\right), \quad (2.1)$$

where  $t$  is time,  $\tau_{\text{BH}}$  and  $\tau_{\text{F}}$  are the thermal decay times of the borehole and formation signals, respectively, and  $A_{\text{BH}}$  and  $A_{\text{F}}$  are the corresponding amplitudes. Although magnetic resonance-like inversion techniques have been recently introduced to extract  $\tau_{\text{F}}$  from  $M(t)$  (Flaum et al., 2008), such linear regressions may not correctly discriminate closely-spaced signals, such as a high- $\Sigma$  formation and an average saline borehole. Instead, we approach the problem with a nonlinear, two-exponential-decay fit, based on the Levenberg-Marquardt algorithm (Marquardt, 1963). This enables the dynamic fit of both borehole and formation responses. All the synthetic Longhorn-PNC-tool measurements reported throughout this thesis originate from the application of that technique.

The purpose of this study is twofold: (a) to rapidly simulate PNC logs, and (b) to use the forward modeling method to correct for shoulder-bed effects in thinly-bedded formations. Therefore, we restrict the data processing step to discriminating formation from borehole signals; we do not attempt to correct for borehole diffusion and other residual borehole effects. A number of papers (Olesen et al., 1987; Murdoch et al., 1990) provide detailed insight to such complementary corrections.

## **2.4 VARIANCE REDUCTION TECHNIQUES**

Because MCNP-simulated measurements stem from a random sampling method, it is crucial to ascertain their reliability. Besides increasing the number of particle histories, which entails longer CPU times, we improve the simulation statistics via several variance reduction techniques. To that end, we first improved the photon sampling in the vicinity of the detector using a next-event estimator that deterministically biases the angle of collisions. We also defined time importance to improve the neutron and photon flux estimates at late time. Finally, we used iterative mesh-based, energy-dependent weight windows for population control purposes. This method tracks particles in important spatial regions, while ascribing lower significance to particles in unimportant regions. Such a strategy ultimately constructs an estimated space-and-energy importance function: the flux sensitivity function. For each Monte Carlo-simulated measurement, the corresponding

## Chapter 3: Limitations of $\Sigma$ Mixing Laws

### 3.1 LINEAR MIXING LAWS

When all the components (rock matrix, shale, and fluids) are homogeneously distributed in space,  $\Sigma$  obeys a linear mixing law, where each component is weighted by its relative volumetric concentration (Clavier et al., 1971a). For instance, one can write the total capture cross section in a clay-free formation as

$$\Sigma_{total} = (1 - \phi)\Sigma_{ma} + \phi(1 - S_w)\Sigma_h + \phi S_w \Sigma_w, \quad (3.1)$$

where  $\phi$  is porosity,  $S_w$  is water saturation,  $\Sigma_{ma}$ ,  $\Sigma_h$ , and  $\Sigma_w$  are the capture cross sections of the rock matrix, hydrocarbon, and water, respectively. In shaly formations, sigma obeys a linear mixing law similar to equation (3.1) as long as the shale is uniformly distributed in the rock such that the formation remains a homogeneous mixture. This situation occurs in the cases of structural and dispersed shale, for which one can write

$$\Sigma_{total} = C_{sh}\Sigma_{sh} + (1 - C_{sh})\Sigma_s, \quad (3.2)$$

where  $C_{sh}$  is volumetric concentration of shale,  $\Sigma_{sh}$  and  $\Sigma_s$  are the capture cross sections of the shale and non-shale components, respectively.

### 3.2 STIEBER MIXING LAW

In heterogeneous formations, neutrons may be captured more promptly in high- $\Sigma$  layers that act as sinks of neutrons, while they preferentially last longer in lower- $\Sigma$  layers,

as pointed out by Allen et al. (1965) in terms of invaded and virgin zones. This behavior indicates that neutrons have a specific spatial variation in layered formations that does not solely depend on the relative volume of each component. Stieber (1970) proposed to compensate for shale effects using the formula

$$C_{sh}^{Stieber} = \frac{C_{sh}}{3 - 2C_{sh}}, \quad (3.3)$$

in lieu of the linear shale index  $C_{sh}$  included in equation (3.2). The latter formula was determined by trial and error over hundreds of datasets.

### 3.3 PNC MEASUREMENTS IN HETEROGENEOUS FORMATIONS

**Figure 3.1** describes two cases of study that emphasize the shortcomings of conventional mixing laws in heterogeneous formations. **Table 3.1** shows the discrepancies associated with the assumption of the linear and the Stieber nonlinear mixing laws between source and detector. Comparison against MCNP simulations of the Longhorn PNC tool indicates more than 68% error for the former, which stems from its inability to account for the spatial variations of neutron flux in heterogeneous formations. For instance, the relative contribution of shale layers to the measurement is lower than expected based on their thickness in both cases. The discrepancy is especially notorious with dissimilar beds, as illustrated by Case No. 2. The Stieber model yields a reduced error compared to the linear model; nevertheless, because it is an empirical model, it may not be reliable for all formation types. Core data would be required to modify accordingly the tuning constants included in equation (3.3).

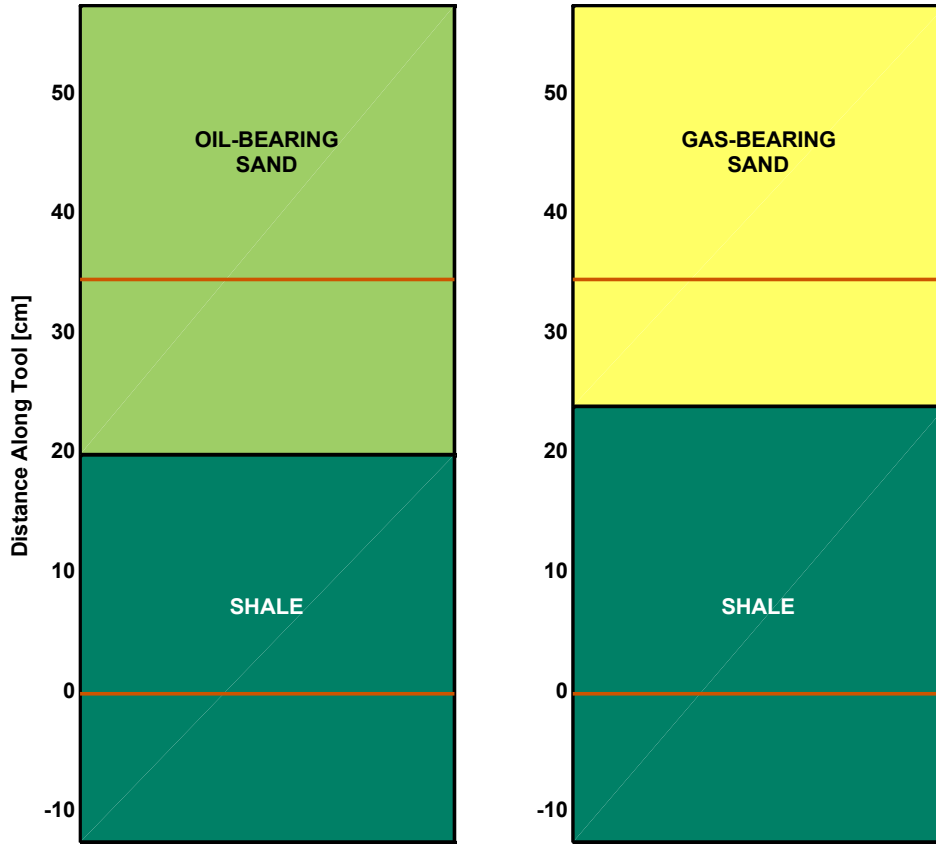


**Figure 3.1:** Case No. 1 (left) consists of a 48.2-c.u. shale layer overlaid by a 14.3-c.u. oil-bearing sand layer. Case No. 2 (right) consists of the same shale layer below a 6.5-c.u. gas-bearing sand layer. Orange-colored lines at 0 and 35 cm describe the positions of source and detector, respectively.

Case	$\Sigma_{\text{MCNP}}$ [c.u.]	$\Sigma_{\text{Linear}}$ [c.u.]	$\Sigma_{\text{Stieber}}$ [c.u.]	$\Delta\Sigma_{\text{Linear}}$ [%]	$\Delta\Sigma_{\text{Stieber}}$ [%]
1	23.8	36.3	27.2	52.5	14.3
2	22.3	37.6	27.1	68.6	21.5

**Table 3.1:** Formation capture cross section calculated with MCNP simulations of the Longhorn PNC tool  $\Sigma_{\text{MCNP}}$ , compared against estimations from the linear mixing law,  $\Sigma_{\text{Linear}}$ , as well as from the nonlinear Stieber model,  $\Sigma_{\text{Stieber}}$ .  $\Delta\Sigma$  is the error between  $\Sigma_{\text{MCNP}}$  and each of these estimations.

However, when beds become thin enough with respect to the diffusion length  $L_d$ , neutrons flow across them as though they were homogeneously mixed. Consequently, there exists a threshold above which heterogeneities begin to impact the measurement, thereby causing deviations from the linear model. For example, Haley (1995) reported that beds thicker than 10 cm are likely to cause measurement biases in a 34%-porosity, 100-kppm salinity sand-shale laminated formation. Thus, the effective  $\Sigma$  in a layered formation becomes a weighted average of the  $\Sigma$  of all the layers that interact with the neutrons. These weights, which represent the importance of each layer toward the effective  $\Sigma$ , are no longer equal to the relative volume of each bed.

## Chapter 4: Formulation of the Problem

By definition, the capture cross section  $\Sigma$  quantifies the ability of a material to capture neutrons. The lower the neutron energy, the more likely capture phenomena will take place, whereby neutrons at thermal energies are the most likely to be absorbed. Consequently, monitoring the population of thermal neutrons provides one with the proper importance function. The total capture cross section  $\Sigma(\mathbf{r})$ , at the detector located at position  $\mathbf{r}$ , is the summation over space of all the cross sections  $\Sigma(\mathbf{r}_0)$  weighted by their flux contribution toward the detector, which is given by the thermal-neutron flux sensitivity function. We approximate this physical interpretation of  $\Sigma$  with the following Fredholm integral equation of the first kind:

$$\Sigma(\mathbf{r}) \approx \int d\mathbf{r}_0 \text{FSF}[\mathbf{r}, \mathbf{r}_0, \Sigma(\mathbf{r}_0)] \Sigma(\mathbf{r}_0), \quad (4.1)$$

where  $\mathbf{r}_0$  is an arbitrary position vector that spans the whole space,  $\Sigma(\mathbf{r}_0)$  is the capture cross section at position  $\mathbf{r}_0$ , and  $\text{FSF}[\mathbf{r}, \mathbf{r}_0, \Sigma(\mathbf{r}_0)]$  is the thermal-neutron flux sensitivity function, which describes the relative contribution of all the  $\Sigma(\mathbf{r}_0)$  at position  $\mathbf{r}$ .

Equation (4.1) is independent of energy in our problem because we assume that all absorbed neutrons are at their thermal energy state. Moreover, for the case of an infinite, homogeneous formation,  $\Sigma(\mathbf{r}_0)$  is constant and independent of  $\mathbf{r}_0$ ; it follows that the FSF must obey the following normalization:

$$\int d\mathbf{r}_0 \text{FSF}[\mathbf{r}, \mathbf{r}_0, \Sigma(\mathbf{r}_0)] = 1. \quad (4.2)$$

We determine the late-time importance of thermal neutrons to ensure cancellation of undesired early-time borehole effects. Furthermore, we assume that fluid re-equilibrium takes place shortly upon setting casing, hence making it possible to neglect invasion effects in the simulation. Also, we assume non-dipping beds. These three assumptions allow us to remove the dependence of the solution of equation (4.1) on the radial and azimuthal directions; the problem is now describable with the vertical direction only. We finally express the total capture cross-section  $\Sigma$  at depth  $z$  as

$$\Sigma(z) \approx \int dz_0 \text{FSF}_{\text{LT}}[z, z_0, \Sigma(z_0)] \Sigma(z_0), \quad (4.3)$$

where  $z_0$  is an arbitrary location that spans the vertical direction,  $\Sigma(z_0)$  is the capture cross section at depth  $z_0$ , and  $\text{FSF}_{\text{LT}}[z, z_0, \Sigma(z_0)]$  is the normalized, radially-averaged, late-time, thermal-neutron flux sensitivity function, which quantifies the relative contribution from all the  $\Sigma(z_0)$  at depth  $z$ .



## Chapter 5: Dependence of FSFs on Formation Properties

### 5.1 HOMOGENEOUS FORMATIONS

Because neutron absorption is uniform everywhere in a homogeneous formation, the FSF merely describes the slowdown of energetic neutrons from the source on their way to the detector. This property explains the smooth, almost-symmetric bell shaped function described in **Figure 5.1**. The FSF is primarily influenced by the slowing-down length  $L_s$ , which is correlated to the hydrogen index  $HI$ . Such a behavior causes potential problems in low-porosity and gas-bearing formations. **Figure 5.2** shows the Monte Carlo-derived, thermal-neutron FSFs for 3 homogeneous formations that span the range of  $L_s$  from 13.21 cm to 37.86 cm; **Table 5.1** reports volumetric compositions and other petrophysical properties of interest for each case of study. Calculated FSFs in low- $HI$  formations are shifted toward the detector because neutrons scatter longer before thermalization and absorption.

Changes of  $\Sigma$  cause negligible effects on FSFs for a similar value of  $L_s$ . **Figure 5.3** compares Monte Carlo-calculated, thermal-neutron FSFs for homogeneous sandstone formations saturated with either fresh or salt water, for 4 different values of porosity. For each of these 4 sets of cases, both  $L_s$  and the diffusion coefficient  $D$  show comparable values, while  $\Sigma$  exhibits significant variations (**Table 5.2**). Yet, FSFs exhibit negligible changes although  $\Sigma$  may vary from 10.73 c.u. to 37.93 c.u. As noted by Randall et al. (1978), neutron absorbers such as chlorine have a small effect on the slowdown process

as well as on the diffusion of neutrons. In other words, thermal-neutron FSFs depend marginally on  $\Sigma$  when absorption is uniform within the volume of investigation.

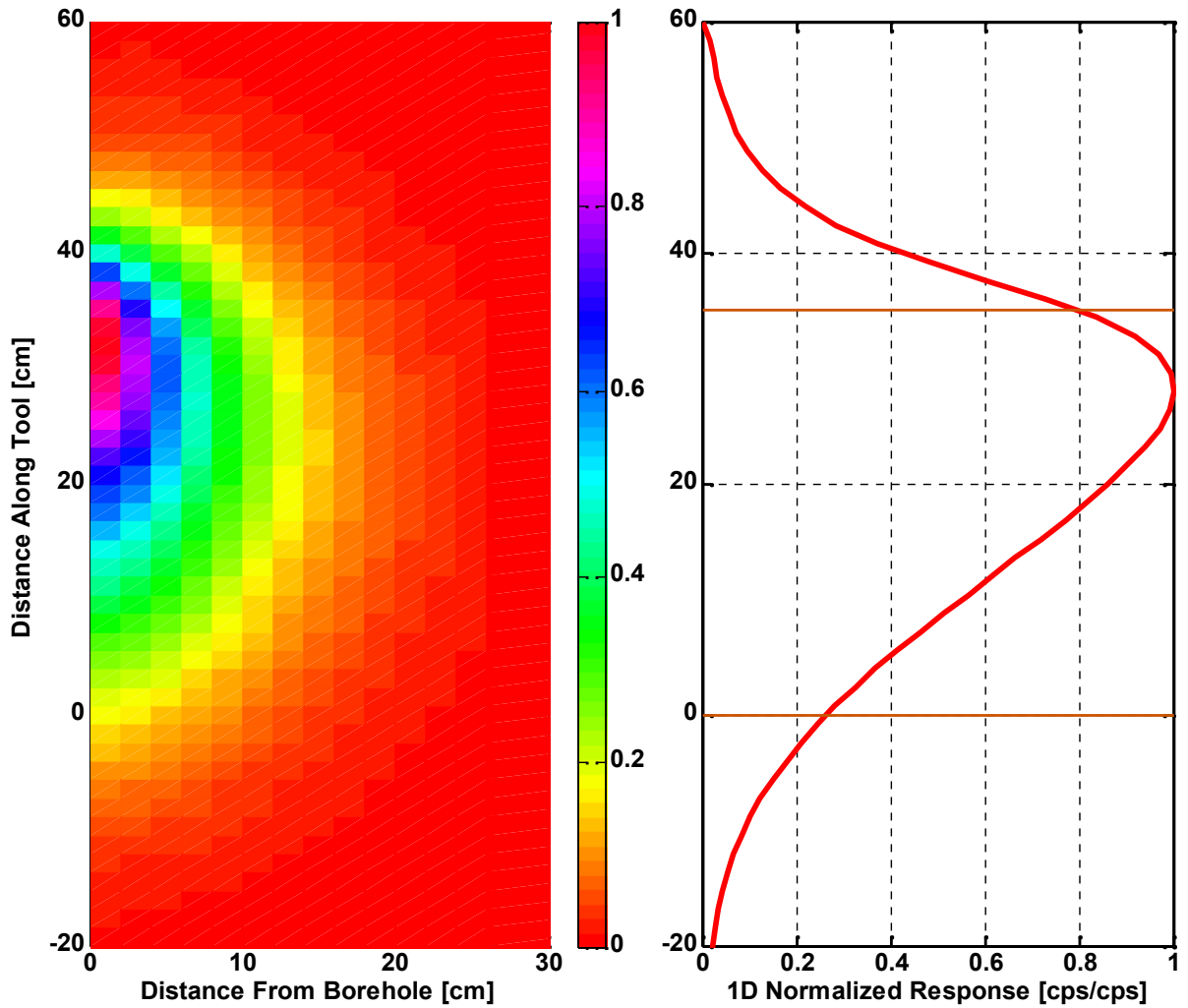


**Figure 5.1:** Thermal-neutron FSF corresponding to PNC measurements acquired with the Longhorn tool in a 25-% porosity sandstone formation saturated with fresh water. The left panel shows the 2D spatial sensitivity of PNC measurements in the formation, and the right panel describes the corresponding 1D plot along the borehole tool, integrated in the radial direction. Orange-colored lines at 0 and 35 cm indicate the positions of source and detector, respectively. For plotting purposes, the FSF was normalized to show variations between 0 and 1. The borehole configuration is: 25.4-cm borehole diameter, 1.78-cm casing and 250-kppm salt water.

Formation	Volumetric composition [ ]	$\phi$ [%]	$\rho_b$ [g/cm <sup>3</sup> ]	$HI$ [ ]	$L_s$ [cm]	$\Sigma_{int}$ [c.u.]
1	0.40 H <sub>2</sub> O, 0.60 SiO <sub>2</sub>	40	1.99	0.40	13.21	11.61
2	0.05 H <sub>2</sub> O, 0.95 SiO <sub>2</sub>	5	2.57	0.05	20.36	5.43
3	0.40 CH <sub>4</sub> , 0.60 SiO <sub>2</sub>	40	1.60	0.01	37.86	3.07

**Table 5.1:** Summary of the assumed lithology and saturating fluid, porosity  $\phi$ , bulk density  $\rho_b$ , hydrogen index  $HI$ , slowing-down length  $L_s$ , and intrinsic capture cross section  $\Sigma_{int}$ , for the 3 formations whose FSFs are reported in Figure 5.2. SNUPAR (McKeon and Scott, 1989) was used to calculate  $L_s$  and  $\Sigma_{int}$ .

$\phi$ [%]	Formation	$L_s$ [cm]	$D$ [cm]	$\Sigma_{int}$ [c.u.]
5	A	20.4	1.02	5.43
	B	20.7	1.03	9.32
15	A	16.0	0.63	7.20
	B	16.3	0.65	18.86
25	A	14.4	0.46	8.97
	B	14.6	0.47	28.4
35	A	13.5	0.36	10.73
	B	13.7	0.37	37.93

**Table 5.2:** Summary of the assumed petrophysical properties for the 8 cases whose FSFs are reported in Figure 5.3. The formations consist of a homogeneous sandstone layer, saturated either with fresh water (Formation “A”) or with 200-kppm salt water (Formation “B”). Slowing-down length  $L_s$ , diffusion coefficient  $D$ , and intrinsic capture cross section  $\Sigma_{int}$  were calculated with SNUPAR.

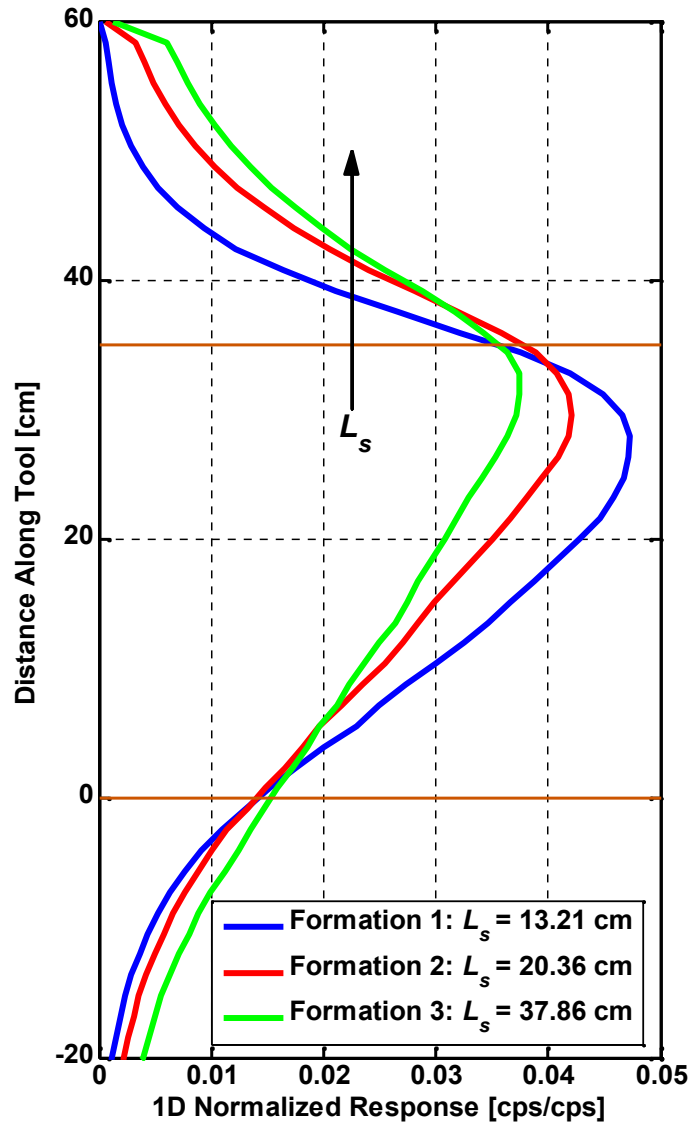


**Figure 5.2:** Impact of slowing-down length  $L_s$  on the spatial sensitivity of PNC measurements acquired with the Longhorn tool, with source and detectors located as indicated by the orange-colored lines at 0 and 35 cm, respectively. Simulations assume a common borehole configuration for all 3 cases: 25.4-cm borehole diameter, 17.8-cm casing diameter and 250-kppm borehole fluid. Unlike in Figure 5.1, the normalization was done according to equation (4.2).

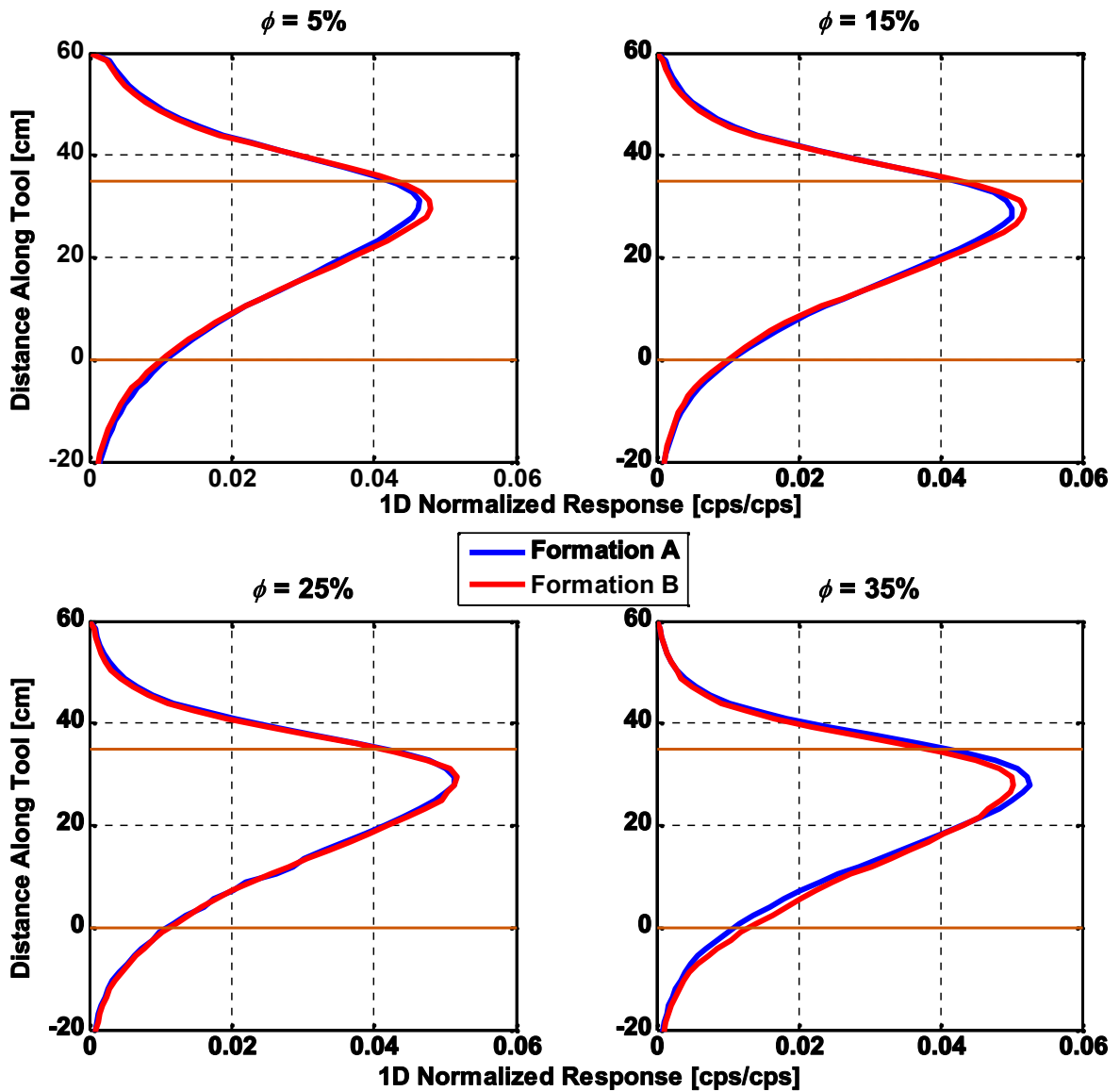


**Figure 5.3:** Impact of  $\Sigma$  on the spatial sensitivity of PNC measurements acquired with the Longhorn tool in homogeneous formations. Blue and red lines represent the thermal-neutron FSFs for a homogeneous sand layer, either saturated with fresh water or with 250-kppm salt water, respectively. Porosity varies from 5% (top left panel) to 35% (bottom right panel). Orange-colored lines at 0 and 35 cm describe the positions of source and detector, respectively. Simulations assume a common borehole configuration for all 3 cases: 25.4-cm-diameter borehole, 17.8-cm-diameter casing and 250-kppm borehole fluid. Normalization was implemented according to equation (4.2).

## 5.2 IMPACT OF HETEROGENEITIES

**Figure 5.4** compares the thermal-neutron FSFs in homogeneous and heterogeneous formations for the same cases displayed in Figure 3.1. The transition between two distinct materials causes distortions in the FSF. Because absorption is no longer uniform in such layered formations, thermal neutrons are more likely to last longer in low- $\Sigma$  materials, while they are absorbed more promptly in higher- $\Sigma$  materials. Indeed, we observe that the flux undergoes a contraction in the high- $\Sigma$  shale and a relaxation in the lower- $\Sigma$  sand layer. Although one can anticipate such changes on qualitative grounds, quantifying them is not trivial. Even though the gas-bearing sand layer has a lower  $\Sigma$  than the oil-bearing layer, the dynamic variations are greater for the latter owing to the impact of the tool position with respect to the layer boundary.

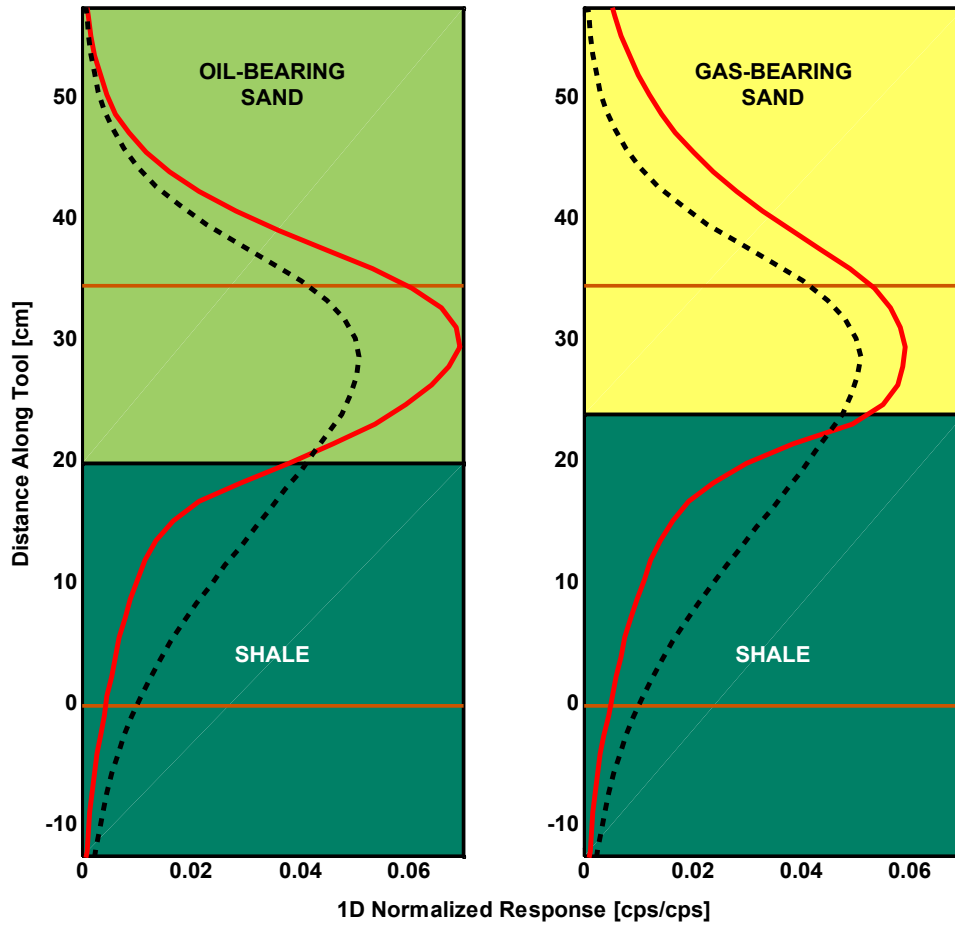


**Figure 5.4:** Comparison of MCNP-generated thermal-neutron FSFs for the layered formation (solid red line) against the FSF for a homogeneous formation (dashed black line), for Cases Nos. 1 (left panel) and 2 (right panel). Orange-colored lines at 0 and 35 cm indicate the location of source and detector, respectively. Normalization was implemented in agreement with equation (4.2).

### 5.3 RADIAL LENGTH OF INVESTIGATION

The above-defined FSFs describe the importance of particle distribution in the radial direction, which is essential to estimate the radial depth of investigation of PNC measurements. **Figure 5.5** shows the radial J-factor (Sherman and Locke, 1975) as a function of the radial distance from the borehole wall for the 6 different cases reported in **Table 5.3**. For 90% of the response, the J-factor exhibits variations of 3.8 cm between low- and high- $\Sigma$  formations. It is found that the size and properties of the borehole do not cause significant impact on the J-factor. The total length of investigation equals 26 cm, which is similar to the result of 26.7 cm reported by Hopkinson et al. (1974). Careful consideration of radial length of investigation is recommended to prevent misleading interpretations of PNC logs in invaded formations (Allen et al., 1965), although cased-hole cases are less likely to be influenced by invasion (Clavier et al., 1971a).

Case	Lithology	$\Sigma_{int}$ [c.u.]	Borehole diameter [cm]	Casing diameter [cm]
1	20%-porosity oil-bearing clean sandstone	9.4	25.4	Openhole
2			25.4	17.8
3			30.5	24.4
4	10%-porosity shale saturated with 200-kppm salt water	49.1	25.4	Openhole
5			25.4	17.8
6			30.5	24.4

**Table 5.3:** Summary of the assumed petrophysical and borehole geometry properties for the 6 cases whose radial J-factors are reported in Figure 5.5. Borehole salinity of 250 kppm is common to all 6 cases.  $\Sigma_{int}$  was calculated with SNUPAR.



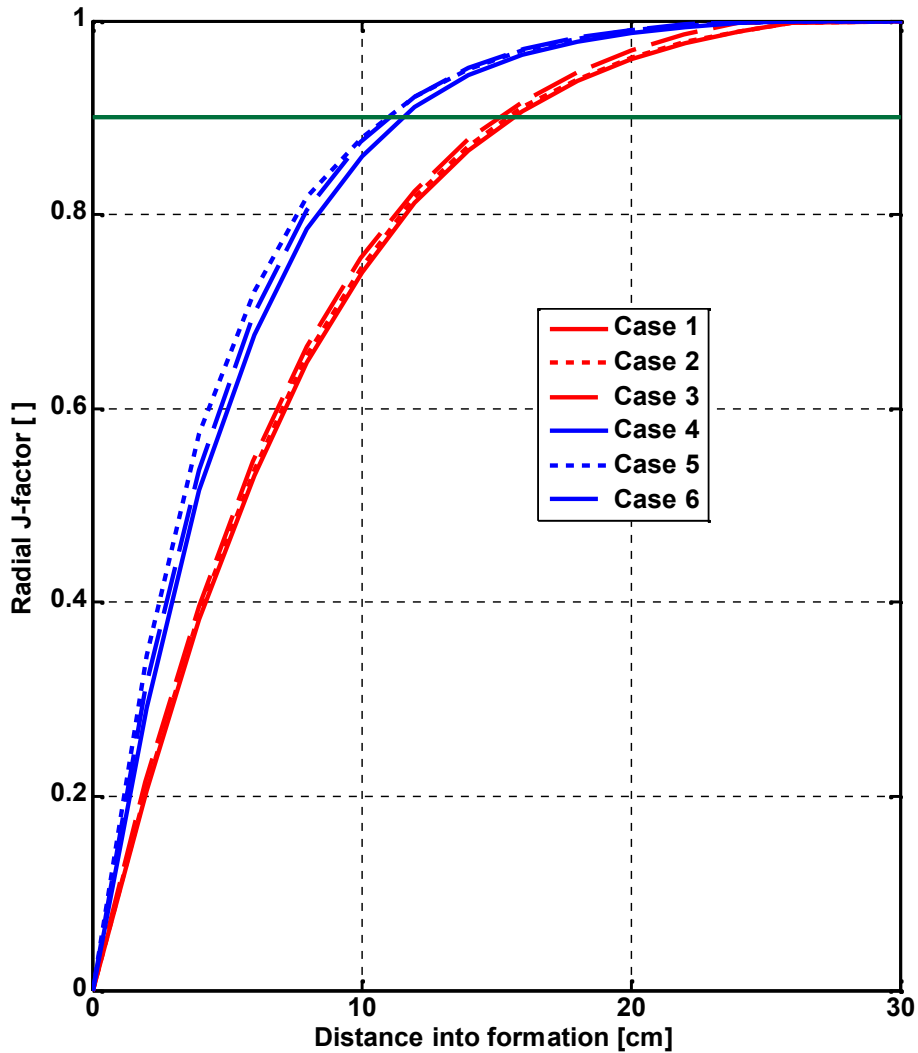


**Figure 5.5:** Radial J-factors of the FSFs for 6 different cases. Red and blue lines describe the geometric factors for oil-bearing sand and shale formations, respectively. Solid lines identify the case of a 25.4-cm-diameter openhole. Dotted lines describe the case of a 25.4-cm-diameter borehole and 17.8-cm-diameter casing configuration. Dashed lines assume a 30.5-cm-diameter borehole, 24.4-cm-diameter casing. The green line identifies the radial length of investigation in the sense of Sherman and Locke (1975), i.e. the 90% value of the radial J-factor.

## Chapter 6: Fast Numerical Simulation of PNC logs

### 6.1 METHOD

Equation (4.3) is the basis for simulating sigma logs. Finding a solution of this equation based on the linear, first-order Born approximation, as already successfully done for neutron and density measurements by Mendoza et al. (2010), is not applicable to our study. Because FSFs are highly dependent on the neutron absorption properties of layered media, the recursive solution of equation (4.3) is not efficient with the FSF for a homogenous formation (linear iterative refinement of a first-order Born approximation). Instead, we develop a solution based on the distorted Born approximation wherein each measurement point is associated with a FSF specific to the *local* multi-layer model in the vicinity of the measurement point, here termed  $\text{FSF}_{\text{LT}}[z, z_0, \Sigma(z_0)]$ . Generating these local FSFs via Monte Carlo simulations requires time-consuming computations, hence the need for a faster method. Likewise, generating these FSFs in advance and constructing a comprehensive library of FSFs in heterogeneous formations is not practical either: one would need to compute as many FSFs as there are heterogeneous cases ( $\Sigma$ , bed thickness, and tool position with respect to the layered formation are all variable parameters). The resulting method would be cumbersome and difficult to implement.

The procedure adopted in this study for the calculation of local FSFs in conjunction with equation (4.3) is based on an initial FSF derived for a homogenous (base-case) formation (which also includes borehole, casing, and cement environmental effects) via

Monte Carlo simulation methods. The initial FSF remains constant for all measurement points as long as the borehole environmental conditions are uniform. Subsequently, the latter FSF is modified to account for local layer diffusion effects using an analytical correction. Assuming that diffusion theory is valid within the local domain of application simplifies the Boltzmann transport equation, thereby allowing us to account for formation heterogeneities analytically. Relevant details about this correction procedure, the underlying assumptions, as well as comparisons between Monte Carlo-computed and diffusion-corrected FSFs are included in Appendix A. Upon correcting the FSFs for local, multi-layer diffusion effects, we use equation (4.3) to determine  $\Sigma$  at each tool position, from which we numerically simulate the PNC log. The analytical nature of the correction of multi-layer diffusion effects enables its implementation within negligible CPU times on a standard PC.

## **6.2 TRANSPORT OF GAMMA RAYS**

The above-described method exclusively concentrates on the transport of neutrons, disregarding the subsequent transport of gamma rays. This approximation is justified by the physics governing the phenomenon of pulsed neutron capture in heterogeneous formations, independently of the detection system, i.e., thermal neutron or capture gamma rays (Allen et al., 1965). Both neutron and photon count rates yield similar values of  $\Sigma$  (Wahl et al., 1970): neutron and photon fluxes are proportional, and there is no delay between neutron capture and gamma ray emission because photons travel at the speed of light (Locke and Smith, 1975). Nevertheless, the choice of acquisition was ultimately

directed toward gamma-ray detection because of its superior radial length of investigation and the greater efficiency of photon detectors. Because the transport of gamma rays in rock formations does not vary significantly from one case to another, we assumed that it was similar for all cases in our approximation, thereby eliminating the need for gamma-ray FSFs.

### **6.3 SYNTHETIC CASES**

The two synthetic examples described below are intended as benchmarking exercises to appraise the reliability and accuracy of the procedure described above to rapidly simulate PNC measurements.

#### **6.3.1 Synthetic Case No. 1: Turbidite Formation**

We first evaluate the performance of the simulation method for the case of a turbidite sequence that alternates oil-saturated sand beds and shale layers. Sand layers include bed thickness ranging from 24.4 to 48.8 cm, while shale bed thickness is constant and equal to 24.4 cm. Both sides of the multi-layer model include end members of the sedimentary sequence as thick beds. **Tables 6.1** and **6.2** summarize the lithology, fluid, and geometrical properties assumed for this case of study.

Longhorn-PNC-tool measurements are simulated along the cased and cemented borehole every 7 cm using MCNP. For depth-matching purposes, we use the geometric

center of the FSFs to define the location of the measurement point, thereby generating field-like PNC measurements that serve as reference. These Monte Carlo simulations required more than 180 hours of CPU time (for 47 depth sample points, assuming 4 hours per run) on a Linux server with Intel Itanium 2 1.4-GHz microprocessors.

Lithology	$\phi$ [%]	$S$ [ ]	$C_{wF}$ [kppm]	$\Sigma_{int}$ [c.u.]	$\Sigma_{dif}$ [c.u.]
Shale	10	$S_w = 1$	100	39.52	40.84
Sand	20	$S_w = 0.2$ $S_o = 0.8$	100	9.38	13.31

**Table 6.1:** Summary of the assumed values of total porosity  $\phi$ , saturation  $S$ , formation water salt concentration  $C_{wF}$ , intrinsic capture cross section  $\Sigma_{int}$  (from SNUPAR) and expected measured capture cross section  $\Sigma_{dif}$  (from MCNP) for the sand and shale components of Synthetic Case No. 1.

Variable	Value	Units
Formation oil: carbon weight fraction	0.87	[ ]
Formation oil: hydrogen weight fraction	0.13	[ ]
Formation oil density	0.82	g/cm <sup>3</sup>
Formation gas density	0.017	g/cm <sup>3</sup>
Borehole fluid salt concentration	225	kppm
Borehole fluid capture cross section	111.2	c.u.
Borehole diameter	25.4	cm
Casing diameter	17.8	cm
Sampling rate	7	cm

**Table 6.2:** Summary of the assumed hydrocarbon densities, borehole fluid properties, well geometry and sampling rate for Synthetic Cases No. 1 and 2.

We use equation (4.3) together with the FSF-correction procedure (reported in Appendix A) to simulate numerically the PNC log for this case. **Figure 6.1** compares the corresponding results against those obtained with MCNP. Less than 1 second of CPU time was necessary to obtain PNC measurements in excellent agreement with their Monte Carlo-derived counterparts. The simulation method reliably reproduces the effects of thin beds and the ensuing rapid variations of the  $\Sigma$  log; shoulder-bed effects are reproduced with less than 2.5-c.u. difference.

### **6.3.2 Synthetic Case No. 2: Complex Multi-Layer Formation**

We now examine the capabilities of the method with a 5.2-m synthetic formation consisting of successive sandstone, shale, shaly sand as well as carbonate beds, saturated with gas, oil, fresh water or saline water. In this example,  $\Sigma$  spans the range from 12.41 to 45.55 c.u., with bed thicknesses between 24 and 76 cm. Variations of  $\Sigma$  from one bed to another are from 6.63 (between beds nos. 1 and 2) to 32.65 c.u. (between beds nos. 4 and 5). **Table 6.3** summarizes the petrophysical information about this case, whereas Table 6.2 reports the borehole fluid properties, well geometry information as well as the hydrocarbon densities involved.

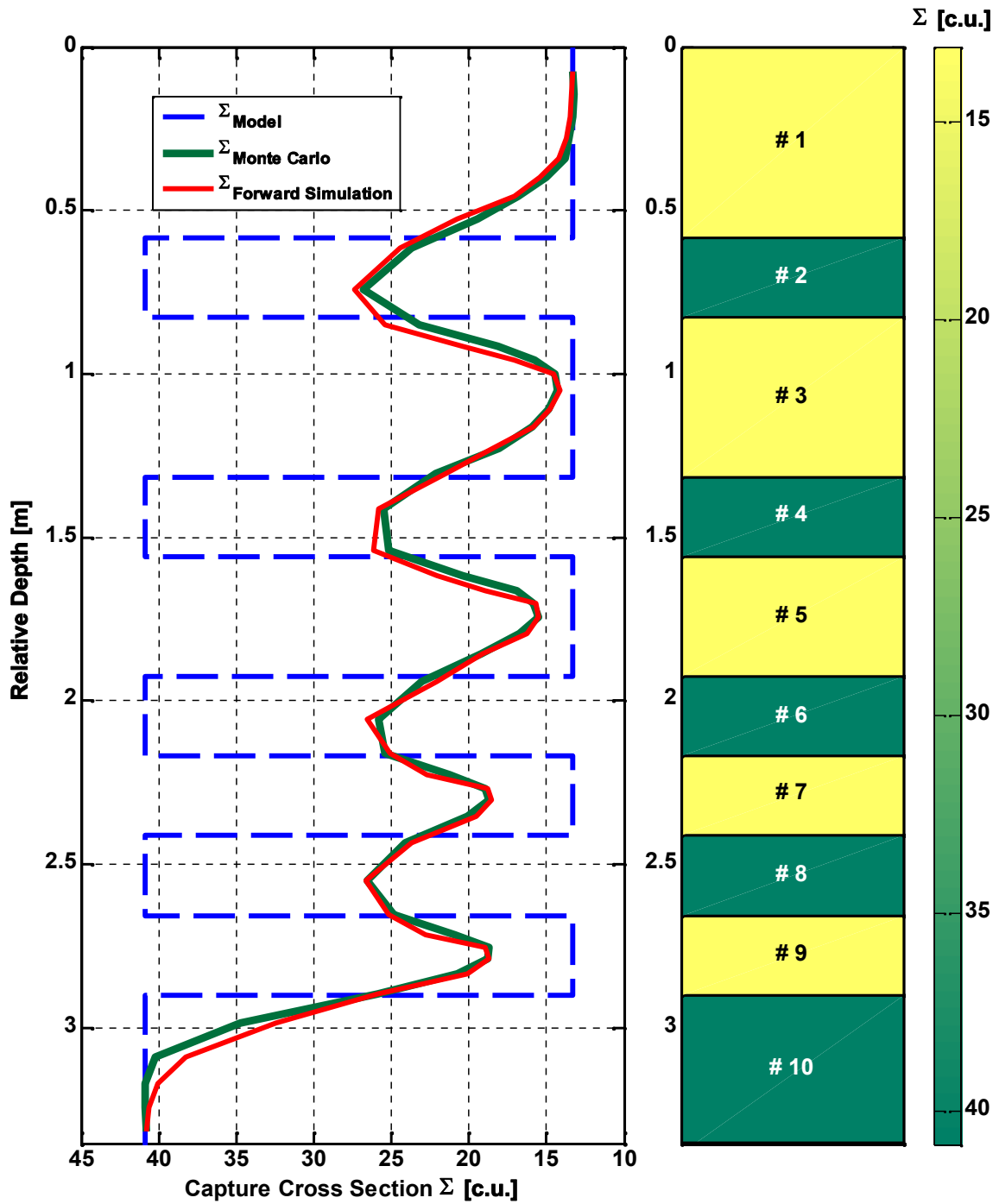


**Figure 6.1:** Comparison of numerically simulated (solid red line) and measured  $\Sigma$  logs (solid green line, calculated with MCNP) for Synthetic Case No. 1. Actual layer-by-layer values are described with the dashed blue line.

#	Lithology	$2H$ [cm]	$\phi_s$ [%]	$\phi_{sh}$ [%]	$C_{sh}$ [ ]	$S_w$ [ ]	$C_{wF}$ [kppm]	HC	$L_s$ [cm]	$\Sigma_{int}$ [c.u.]	$\Sigma_{dif}$ [c.u.]
1	Limestone	70.1	5	–	–	0.4	150	Gas	22.1	8.32	12.41
2	Dolomite	67.1	12	–	–	0.65	250	Oil	14.8	14.60	19.04
3	Shale	39.6	–	10	1	1	200	–	10.5	41.86	45.55
4	Sandstone	24.4	20	–	–	0.4	50	Oil	15.1	9.38	12.90
5	Shale	76.2	–	10	1	1	200	–	10.5	41.86	45.55
6	Shaly Sand	61	10	10	0.6	0.5	100	Gas	15.0	11.99	15.21
7	Shaly Sand	45.7	15	10	0.3	0.7	150	Oil	14.8	17.75	20.95
8	Sandstone	30.5	20	–	–	0.4	50	Oil	15.1	9.38	12.90
9	Sandstone	45.7	25	–	–	1	220	–	14.6	30.63	31.69
10	Sandstone	57.9	25	–	–	1	0	–	14.4	8.96	11.65

**Table 6.3:** Summary for Synthetic Case No. 2 of the assumed lithology, bed thickness  $2H$ , non-shale porosity  $\phi_s$ , shale porosity  $\phi_{sh}$ , volumetric concentration of shale  $C_{sh}$ , water saturation  $S_w$ , formation water salt concentration  $C_{wF}$ , nature of the hydrocarbons HC, slowing-down length  $L_s$  (from SNUPAR), intrinsic capture cross section  $\Sigma_{int}$  (from SNUPAR), and expected measured capture cross section  $\Sigma_{dif}$  (from MCNP simulations of the pure, infinite-extent formation in the presence of the borehole), from top to bottom of the formation.



**Figure 6.2** compares the numerically simulated log against the Monte Carlo reference log that was obtained in a similar fashion as reported for Synthetic Case No. 1, for a total of 300 hours of CPU time (for 74 depth sample points). Our simulation method required less than 1 second of CPU time to reliably reproduce the variations of the measured  $\Sigma$  log, yielding a maximum difference of 2 c.u. with respect to the Monte Carlo-simulated measurements for the transitions between similar materials. By contrast, the transition between the low- $\Sigma$  bed no. 4 and the high- $\Sigma$  bed no. 5 exhibits an error of up to 5-c.u.

It is important to emphasize that the simulations obtained with Monte Carlo methods as described above yield count rates that were subsequently processed to calculate the corresponding PNC logs (as described in a previous section of this thesis). By contrast, our simulation method directly yields sigma values.

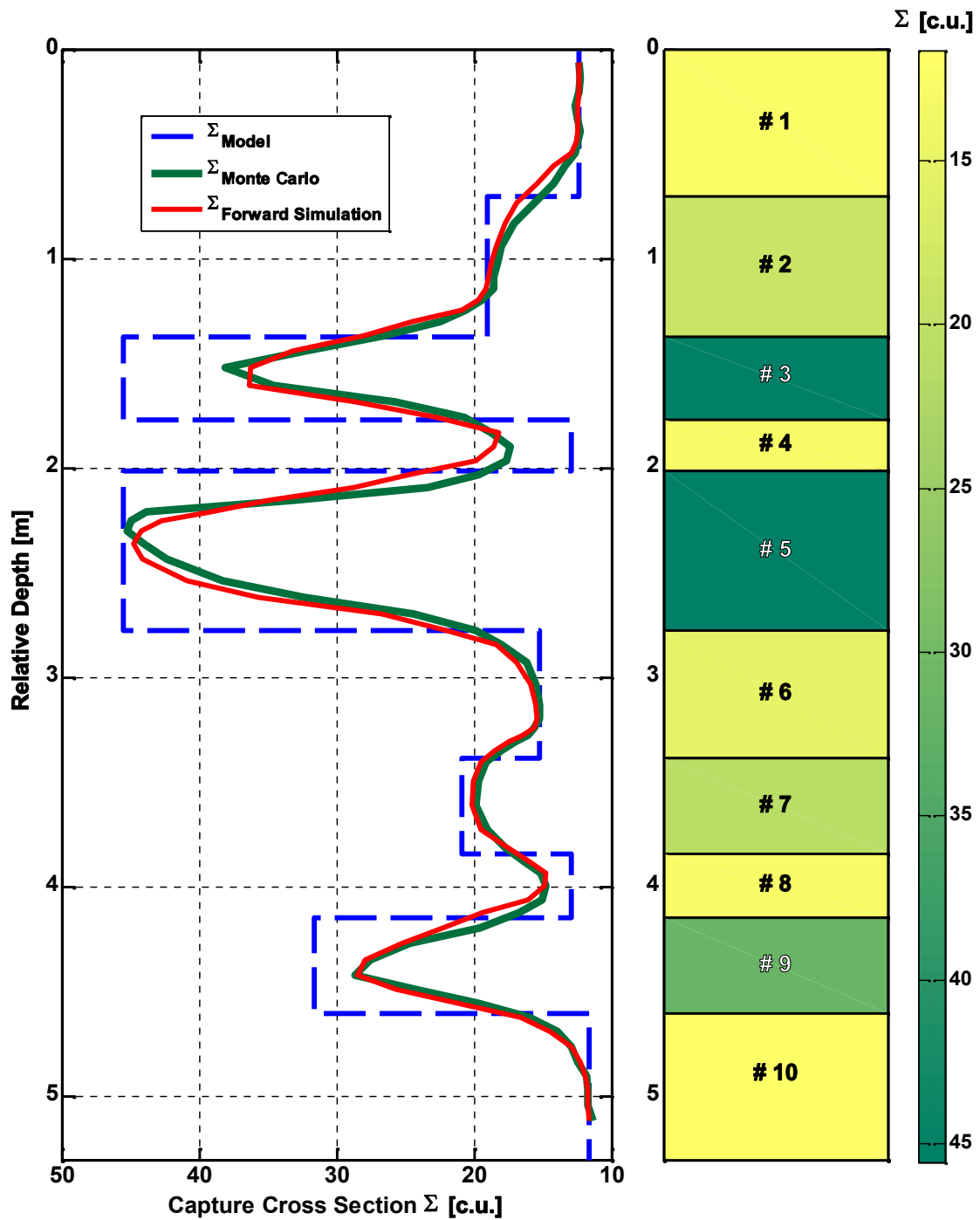


**Figure 6.2:** Comparison of numerically simulated (solid red line) and measured  $\Sigma$  logs (solid green line, calculated with MCNP) for Synthetic Case No. 2. Actual layer-by-layer values are described with the dashed blue line.

## Chapter 7: Inversion in Thinly-Bedded Formations

### 7.1 BACKGROUND AND OBJECTIVES

Well logs acquired in thinly-bedded formations often exhibit significant shoulder-bed effects, rendering them spatially smooth. In the specific case of PNC logs, neighboring layers may contribute substantially toward the measured capture cross section  $\Sigma$ , making the interpretation of PNC logs challenging in economic pay zones, and hindering the accurate appraisal of layer-by-layer hydrocarbon saturation. This behavior stems from the continuous diffusion of neutrons between low- and high- $\Sigma$  thin beds. However, it does not affect time-lapse interpretation methods because such effects properly cancel out when differencing the measurements.

A number of previously-published studies address the formulation (Dunn, 1989) and correction (Mickael, 1999) of borehole and ensuing diffusion effects on PNC logs. Empirical techniques (Plasek et al., 1995) have now taken precedence over such complex analytical and numerical solutions. However, no interpretation schemes have been advanced to account for diffusion effects that take place in heterogeneous formations. To date, only Monte Carlo techniques have the necessary accuracy and versatility to model nuclear borehole measurements such as PNC logs (Butler, 1987). This is achieved at the expense of computationally intensive simulations, thereby preventing their systematic use within an inversion framework.

The limitation of CPU-intensive calculations is not specific to PNC measurements but is actually common to all nuclear borehole measurements. The extensive work recently carried out in this area has led to the formulation of fast, approximate, yet accurate, numerical simulation methods of density (Zhou et al., 2009; Mendoza et al., 2010) and neutron measurements (Wiley and Patchett, 1990; Ellis and Chiaramonte, 2000; Guo and Wang, 2009; Mendoza et al., 2010), for their subsequent use with inversion techniques (Patchett and Wiley, 1994; Aristodemou et al., 2006; Carmine et al., 2008; Mendoza et al., 2009).

The objective of this paper is to develop a new method to estimate layer-by-layer values of  $\Sigma$  from borehole PNC measurements. To that end, we make use of the previously introduced fast simulation of PNC borehole measurements (Mimoun et al., 2010). The simulation method resorts to Monte Carlo-calculated geometric response factors –referred to as flux sensitivity functions (FSFs)–, together with a 1D (vertical) neutron-diffusion correction. The speed and accuracy of the simulation procedure make it an ideal candidate for integration with an iterative nonlinear inversion algorithm for estimation of layer-by-layer properties.

We specifically aim at applying the inversion procedure to the interpretation of thinly-bedded formations to improve their detection and quantification. Even though multi-layer formations that consist of thick beds exhibit shoulder-bed effects, the measurement log already coincides with the expected value of  $\Sigma$  in the center of each bed. On the other hand, thinly-bedded formations (i.e. with beds thinner or comparable to

neutron diffusion length) behave as though all intra layers were homogeneously mixed (Haley, 1995). Moreover, the vertical resolution of logging tools limits the resolution of beds thinner than 25 to 30 cm. Our study is focused to intermediate cases wherein bed thickness ranges from 24 to 50 cm. In such conditions, the thermal-neutron flux undergoes complex spatial variations that limit reliance on mixing laws. Furthermore, concurrent diffusion effects between dissimilar thin beds cause spatial smoothing of logs that biases their evaluation: hydrocarbon-bearing beds may exhibit higher  $\Sigma$  than expected while water-bearing sands and shales may exhibit lower  $\Sigma$  than expected.

We test the robustness and reliability of the inversion method with two synthetic examples of thinly-bedded formations and three sets of field measurements. The method reduces shoulder-bed effects on PNC logs and sharpens the estimation of layer-by-layer  $\Sigma$  values.

## **7.2 FORMULATION**

### **7.2.1 Petrophysical Framework**

We introduce an iterative method that makes use of the previously developed fast numerical simulation of  $\Sigma$  logs. For consistency purposes, the inversion procedure is subject to the same set of assumptions invoked by the simulation algorithm: (a) subsurface formations may be heterogeneous in the vertical direction only (petrophysical layering is perpendicular to the vertical borehole), (b) PNC data are free of early-time

borehole effects, and (c) the diffusion approximation is valid to describe thermal-neutron-flux variations.

### 7.2.2 Inversion of PNC Logs

We formulate the inverse problem of PNC measurements as the minimization of the quadratic cost function

$$C(\mathbf{x}) = \|\mathbf{e}(\mathbf{x})\|^2 + \lambda^2 \|\mathbf{x}\|^2, \quad (7.1)$$

where  $\mathbf{x}$  is a vector containing the unknown layer-by-layer values of  $\Sigma$ ,  $\mathbf{e}(\mathbf{x})$  is vector of data residuals, and  $\lambda$  is a stabilization (regularization) parameter calculated using Hansen's (1994) L-curve criterion. The vector of data residuals is given by

$$\mathbf{e}(\mathbf{x}) = \begin{bmatrix} e_1(\mathbf{x}) \\ \vdots \\ e_n(\mathbf{x}) \\ \vdots \\ e_N(\mathbf{x}) \end{bmatrix} = \begin{bmatrix} d_1(\mathbf{x}) - d_1^0 \\ \vdots \\ d_n(\mathbf{x}) - d_n^0 \\ \vdots \\ d_N(\mathbf{x}) - d_N^0 \end{bmatrix} = \mathbf{d}(\mathbf{x}) - \mathbf{d}^0, \quad (7.2)$$

where the entry  $e_n(\mathbf{x})$  designates the  $n$ -th data misfit at the  $n$ -th sampling depth  $z_n$ ,  $\mathbf{d}^0$  is an  $N$ -size vector of PNC measurements, and  $\mathbf{d}(\mathbf{x})$  is the  $N$ -size vector of numerically simulated  $\Sigma$  measurements. We determine  $\mathbf{d}(\mathbf{x})$  with the fast numerical simulation method applied to  $\mathbf{x}$ ; at the  $n$ -th sampling depth  $z_n$ , it is given by:

$$d_n(\mathbf{x}) = \int dz_0 \mathbf{FSF}[z_n, z_0, \mathbf{x}(z_0)] \mathbf{x}(z_0), \quad (7.3)$$

where  $z_0$  is an arbitrary location that spans the vertical direction and  $\mathbf{FSF}[z_n, z_0, \Sigma(z_0)]$  is the normalized, radially-averaged, late-time, thermal-neutron flux sensitivity function,

which quantifies at depth  $z_n$  the relative contribution from all the layer-by-layer  $\Sigma$  values contained in  $\mathbf{x}$ .

Although equation (7.3) implies a linear relationship between the measurements  $d_n(\mathbf{x})$  and the layer-by-layer model  $\mathbf{x}(z_0)$  at a given sampling depth  $z_n$ , FSFs are in general depth variant in heterogeneous formations. Therefore, we describe the mapping between model  $\mathbf{x}$  and data  $\mathbf{d}$  with a nonlinear system of equations that we solve using the Levenberg-Marquardt method (Marquardt, 1963). At every iteration, we numerically compute the Jacobian matrix that consists of all first-order partial derivatives of  $\mathbf{d}$  with respect to  $\mathbf{x}$ . We subsequently determine the incremental variation of model parameters  $\mathbf{x}$  by minimizing the quadratic cost function previously defined in equation (7.1).

### 7.2.3 Iterative Inversion Algorithm

**Figure 7.1** summarizes the workflow adopted in this study to appraise unknown layer-by-layer values of  $\Sigma$ . The method first detects bed boundaries from the inflection points of a master log (gamma-ray, density, neutron or resistivity logs if open-hole data are available, otherwise we use the PNC log itself). Next, the layered model may be initialized with values of  $\Sigma$  determined from the measured log: successive minima and maxima of the smooth log provide a reliable first guess. Alternatively, the average value of the log is a parsimonious, yet efficient choice.

From the corresponding corrected FSFs and the measurements, we construct a nonlinear system of equations that yields updated model parameters  $\mathbf{x}$ , which

subsequently become the new initial guess to populate the layered model. Convergence of this iterative procedure is diagnosed by comparing the variations of model parameters,  $\Delta \mathbf{x}$ , from one iteration to the next against a pre-specified threshold. We also compare the measured log,  $\mathbf{d}^0$ , against the numerically simulated log,  $\mathbf{d}(\mathbf{x})$ , rendered by equation 3.

Additionally, we appraise the uncertainty of the estimated layer-by-layer  $\Sigma$  values from the 95% confidence interval of the model covariance matrix that results from a perturbation of the measurement log. In so doing, we assess the influence of noise on model estimates, which we plot as error bars together with the inverted model. Moreover, we investigate the impact of initial guess and bed-boundary location on the solution.



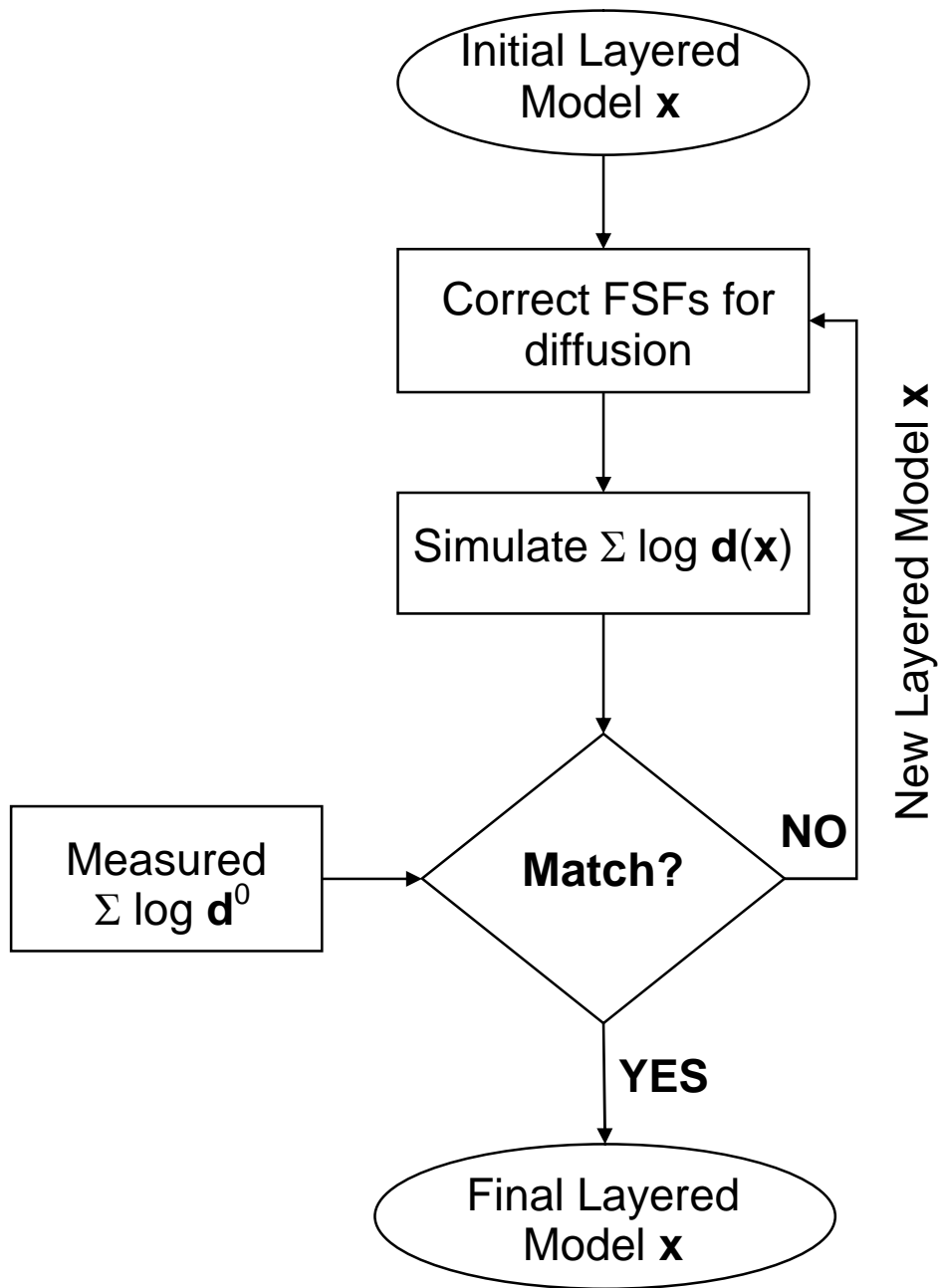


**Figure 7.1:** Flowchart of the fast-forward and inversion method developed for PNC logs. The agreement (match) between numerical simulations and measurements is ascertained from the increment in model parameters from one iteration to the next, which is verified against a pre-specified threshold.

### 7.3 SYNTHETIC EXAMPLES

We evaluate the robustness of the developed inversion method with the following two examples of synthetic formations.

#### 7.3.1 Synthetic Case No. 3

This synthetic case is intended to reduce variable shoulder-bed effects on the interpretation method. It consists of a 2.40-m siliciclastic sequence with water-, oil- and gas-bearing sand layers, alternated with high- $\Sigma$  shale layers (illite is the dominant clay mineral). **Table 7.1** summarizes the lithology and fluid properties assumed for this case. **Table 7.2** reports complementary borehole fluid properties, well geometry information as well as hydrocarbon densities.

**Figure 7.2** displays the numerically simulated PNC log and the final estimates of layer-by-layer  $\Sigma$  values, together with the measurement log and the true model, respectively. The numerical simulation reliably reproduces the PNC measurements acquired along depth intervals within shale, oil-bearing and water-bearing layers, where input and numerically simulated (resulting from inversion) logs agree within less than 1.3-c.u. This lower section from 0.70 to 2.40 m comprises materials with similar slowing-down lengths, thereby allowing the use of a single base-case FSF to perform the numerical simulations. However, presence of gas in the upper section causes a small mismatch when modeling PNC measurements acquired in the vicinity of layer no. 2 (from 0.30 to 0.70 m), with errors up to 3.8 c.u. This behavior takes place despite the

implementation of a specific correction for the presence gas during the rapid simulation because the method does not gradually shift the regular base-case FSF to a gas-specific FSF when the logging point is located in the vicinity of the gas-bearing sand.

Shoulder-bed effects and spatial smoothing of the PNC log may cause significant misinterpretations, especially in thin beds. For instance, the shale layer no. 3 shows a peak at 30.1 c.u. only, i.e. 19.5 c.u. below the actual value of 49.6 c.u. Likewise, the transition from the water leg (layer no. 6) to the overlying shale (layer no. 5) does not show the actual 16.7-c.u. difference but only an increase of 2 c.u. When using the average value of the measurement log (equal to 33.1 c.u.) as the initial guess, the iterative procedure converges to final results in seconds of CPU time and culminates in the reconciliation of the true  $\Sigma$  model properties and the estimated inverted  $\Sigma$  properties. Across hydrocarbon-bearing beds, the difference between input and numerically simulated logs is less than 0.30-c.u. **Table 7.3** reports for each layer the errors between estimated and actual model parameters, as well as the 95% confidence interval for a perturbation of the measurement log of 2%. Uncertainty of inversion results across shale layers is larger than across sand layers. This behavior stems from the properties of late-time, thermal-neutron FSFs in heterogeneous formations: they “stretch” in lower- $\Sigma$  layers (such as hydrocarbon-bearing formations) and “contract” in higher- $\Sigma$  layers (such as water legs and shale), thus why the relatively low sensitivity of the measurements to high- $\Sigma$  layers, especially across thin beds. Once the tool logs the thick shale layers nos. 1 and 7, the low- $\Sigma$  sand beds no longer influence the measurement and we infer the model

values with less than 4% uncertainty. By comparison, inversion results for the low- $\Sigma$  sand layers nos. 2, 4, and 6 are more stable, even with bed thickness as low as 24.4 cm.

The inversion algorithm converges independently of the initial guess: initializations either from the smooth log or from parsimonious guesses (constant average value of the log as well as shale assumed everywhere) yield the same outcome: in this case the solution to the inverse problem is not severely nonunique as long as the initial guess remains physically consistent (no zero or negative values for instance).

#	Lithology	$2H$ [cm]	$\phi$ [%]	$S$ [ ]	$C_{wF}$ [kppm]	$\Sigma_{int}$ [c.u.]
1	Shale	55	35	$S_w = 1$	215	48.2
2	Sand	40	25	$S_w = 0.1$ $S_g = 0.9$	200	6.47
3	Shale	25	35	$S_w = 1$	215	48.2
4	Sand	35	30	$S_w = 0.2$ $S_o = 0.8$	200	14.3
5	Shale	25	35	$S_w = 1$	215	48.2
6	Sand	25	35	$S_w = 1$	200	28.4
7	Shale	35	35	$S_w = 1$	215	48.2

**Table 7.1:** Summary of the assumed lithology, bed thickness  $2H$ , total porosity  $\phi$ , saturation  $S$ , formation water salt concentration  $C_{wF}$ , and intrinsic capture cross section  $\Sigma_{int}$  for Synthetic Case No. 3, from top to bottom of the formation.  $\Sigma_{int}$  was determined from SNUPAR.

Variable	Value	Units
Formation oil: carbon weight fraction	0.87	[ ]
Formation oil: hydrogen weight fraction	0.13	[ ]
Formation oil density	0.82	g/cm <sup>3</sup>
Formation oil capture cross section	21.3	c.u.
Formation gas density	0.017	g/cm <sup>3</sup>
Formation gas capture cross section	0.85	c.u.
Borehole fluid salt concentration	225	kppm
Borehole fluid capture cross section	111.2	c.u.
Borehole diameter	25.4	cm
Casing diameter	17.8	cm
Sampling rate	7	cm

**Table 7.2:** Summary of the assumed hydrocarbon densities, borehole fluid properties, well geometry and sampling rate for Synthetic Cases Nos. 3 and 4.

#	Lithology	$\Sigma_{dif}$ [c.u.]	$\Sigma_{est}$ [c.u.]	$\Delta\Sigma$ [c.u.]	$\Delta\Sigma$ [%]	$\delta\Sigma_{95}$ [%]
1	Shale	49.6	52.7	3.1	6.2	3.5
2	Sand	10.6	10.7	0.1	1.2	11.2
3	Shale	49.6	50.0	0.4	0.9	26.6
4	Sand	18.2	17.9	-0.3	-1.7	9.6
5	Shale	49.6	52.2	2.6	5.2	15.4
6	Sand	32.9	33.7	0.8	2.4	7.2
7	Shale	49.6	50.7	1.1	2.3	5.2

**Table 7.3:** Final layer-by-layer capture cross sections  $\Sigma_{est}$  estimated upon matching the measured log with fast-forward simulations, from top to bottom of the formation, for Synthetic Case No. 3.  $\Sigma_{dif}$  is the expected measured capture cross section (from MCNP).  $\Delta\Sigma$  is the error (both absolute and relative) between  $\Sigma_{est}$  and  $\Sigma_{dif}$ .  $\delta\Sigma_{95}$  quantifies the uncertainty in the appraisal (95% confidence interval).

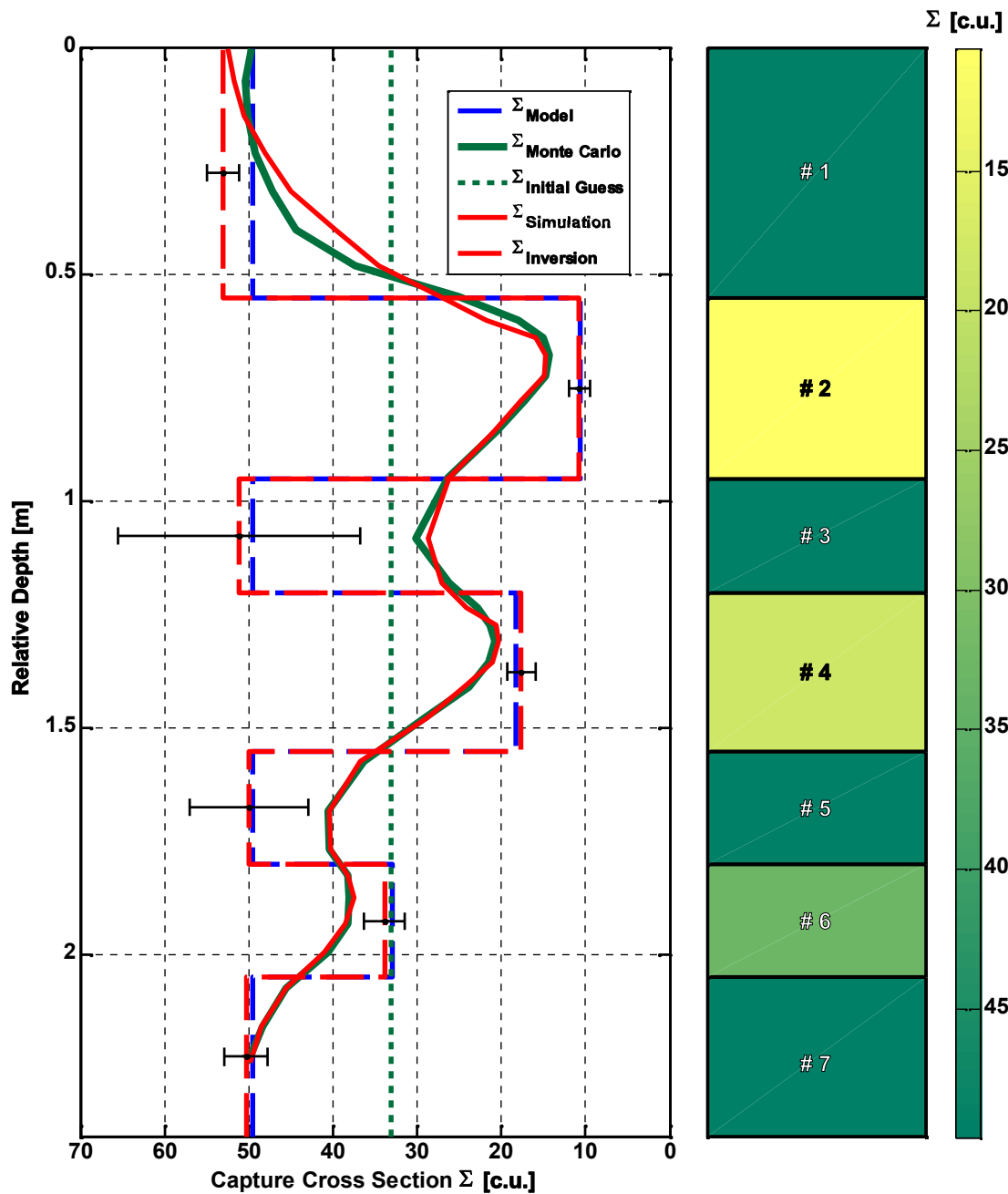


**Figure 7.2:** Comparison of estimated layer-by-layer  $\Sigma$  values (dashed red line) and true model values (dashed blue line) for Synthetic Case No. 3. Numerically simulated and measured  $\Sigma$  logs are indicated with solid red and green lines, respectively. The inversion was initialized with a parsimonious guess based on the average value of the measured log (dashed green line). Black error bars describe the 95% confidence interval.

### 7.3.2 Synthetic Case No. 4

This synthetic case investigates the influence of bed thickness on the inversion of PNC logs as well as the impact of noise and bed-boundary perturbations. It consists of a 3.30-m turbidite sequence that alternates low- $\Sigma$ , oil-saturated sand beds and high- $\Sigma$  shale layers (chlorite is the dominant clay mineral). **Table 7.4** summarizes the petrophysical information for the two end-members of this siliciclastic sedimentary sequence exhibiting a sharp contrast in  $\Sigma$ : 13.31 and 40.81 c.u. Borehole fluid properties, well geometry information as well as oil density are the same as those reported in Table 7.2.

**Figure 7.3** shows the numerically simulated PNC log and the final layer-by-layer estimates of  $\Sigma$ , together with the measurement log and the true model, respectively. Numerically simulated and reference logs agree within less than 1.7-c.u.; 10 iterations and 10 seconds of CPU time are necessary to reach convergence of the iterative algorithm.

Even though the fluid and mineral composition of oil-bearing sand layers does not change with depth, changes in bed thickness bias their evaluations from the measured log. While the thick, 57.9-cm, layer no. 1 displays the expected value of 13.31 c.u.,  $\Sigma$  increases up to 18.75 c.u. in the center of the 24.4-cm layers nos. 7 and 9, owing to substantial shale-sand diffusion effects. Such a behavior may cause a significant bias in the calculation of fluid saturation for these thin sand layers.

Similarly to Synthetic Case No. 3, we use the average value of the measurement log (equal to 21.55 c.u.) to initialize the iterative inversion algorithm. Upon completion, the inverted formation properties match the actual model  $\Sigma$  values within less than 0.5-c.u. error for the hydrocarbon-bearing sand layers. This difference is not significant given the PNC reproducibility of 0.5 to 1.0 c.u. (Kimminau and Plasek, 1992). **Table 7.5** displays for each layer the errors between estimated and actual model parameters, as well as the 95% confidence interval for a 2% perturbation of the measured log. As already observed in Synthetic Case No. 3, the loss of measurement sensitivity in shale layers results in a mismatch (up to 3.16 c.u.) and a larger uncertainty (up to 14.2%) in the estimated  $\Sigma$  values.

We now appraise the stability of the inversion by adding synthetic noise to the PNC data. In addition to the presence of Poisson statistical noise in borehole nuclear measurements that originates from the finite number of gamma ray counts, there exist borehole and completion effects, perturbation in tool calibration, and other disturbances from the operational logging environment that cause errors in the measured log (Kimminau and Plasek, 1992). Thus, we add 5% random biased noise to the Monte Carlo-simulated  $\Sigma$  log prior to performing the inversion. The match between rapidly simulated and noisy measurement logs shows an average difference of 21.4% with respect to the agreement previously reached with noise-free data. Because the log now exhibits anomalous fluctuations and the same number of unknowns remains in the inverse problem, numerical simulations no longer fit the measurements correctly. However, the



inverted layer-by-layer  $\Sigma$  for hydrocarbon-bearing sand beds still shows agreement with true formation properties (errors below 1.5 c.u.)

Even though one may readily correct for depth shifts among logs via cross-correlation methods, ascertaining bed thickness is challenging when using field data. To appraise the effect of erroneous bed boundaries on inversion results, we apply bed-thickness perturbations to the model, with variations below the sampling interval. In so doing, we introduce an inconsistency between the measurements and layer-by-layer values of  $\Sigma$ . In the case of rapid variation of the measured log (as observed between 2 and 3 m), the strong intercorrelation of model parameters misleadingly enables a good match between simulated and measured logs (**Figure 7.4**). Inverted  $\Sigma$  values no longer represent the original system:  $\Sigma$  values in shale layers nos. 2, 4, and 6 are overestimated, while the value of  $\Sigma$  in sand layer no. 9 is estimated at 16.7 c.u. (instead of 13.4 c.u. with correct bed boundaries). This 3.3-c.u. difference causes a discrepancy in saturation evaluation (44 saturation units), thereby emphasizing the importance of accurate bed-boundary selection in the interpretation method, especially in thin beds.

Lithology	$\phi$ [%]	$S$ [ ]	$C_{wF}$ [kppm]	$\Sigma_{int}$ [c.u.]	$\Sigma_{dif}$ [c.u.]
Shale	10	$S_w = 1$	100	39.52	40.84
Sand	20	$S_w = 0.2$ $S_o = 0.8$	100	9.38	13.31

**Table 7.4:** Summary of the assumed values of total porosity  $\phi$ , saturation  $S$ , formation water salt concentration  $C_{wF}$ , intrinsic capture cross section  $\Sigma_{int}$  (from SNUPAR) and expected measured capture cross section  $\Sigma_{dif}$  (from MCNP) for the sand and shale components of Synthetic Case No. 4.

#	Lithology	$2H$ [cm]	$\Sigma_{est}$ [c.u.]	$\Delta\Sigma$ [c.u.]	$\Delta\Sigma$ [%]	$\delta\Sigma_{95}$ [%]
1	Sand	57.9	13.2	-0.14	-1.07	6.05
2	Shale	24.4	37.7	-3.16	-7.74	10.3
3	Sand	48.8	13.2	-0.09	-0.65	6.66
4	Shale	24.4	40.0	-0.85	-2.09	13.1
5	Sand	36.6	13.1	-0.26	-1.95	8.33
6	Shale	24.4	38.5	-2.36	-5.77	13.0
7	Sand	24.4	13.7	0.43	3.25	11.4
8	Shale	24.4	40.0	-0.82	-2.02	14.2
9	Sand	24.4	13.5	0.16	1.20	9.11
10	Shale	45.7	41.8	0.93	2.27	2.59

**Table 7.5:** Final layer-by-layer capture cross sections  $\Sigma_{est}$  estimated by the iterative inversion method applied to Synthetic Case No. 4, from top to bottom of the formation.  $2H$  is bed thickness.  $\Delta\Sigma$  is the error between  $\Sigma_{est}$  and  $\Sigma_{dif}$  (reported in Table 7.4).  $\delta\Sigma_{95}$  quantifies the uncertainty of the appraisal (95% confidence interval).

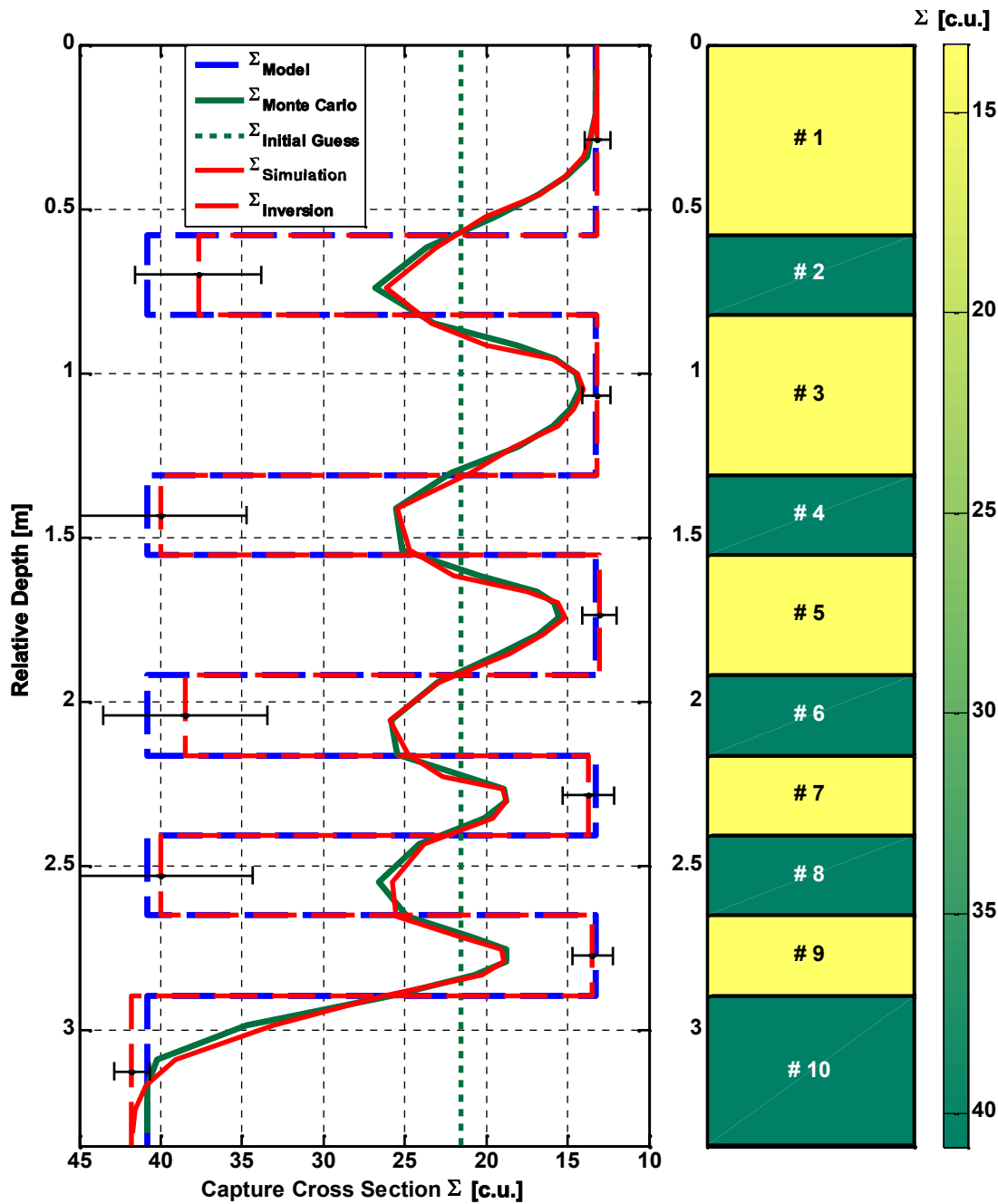


**Figure 7.3:** Comparison of estimated layer-by-layer  $\Sigma$  values (dashed red line) and true model values (dashed blue line) for Synthetic Case No. 4. Numerically and measured  $\Sigma$  logs are indicated with solid red and green lines, respectively. The inversion was initialized with a parsimonious guess based on the average value of the measured log (dashed green line). Black error bars describe the 95% confidence interval.

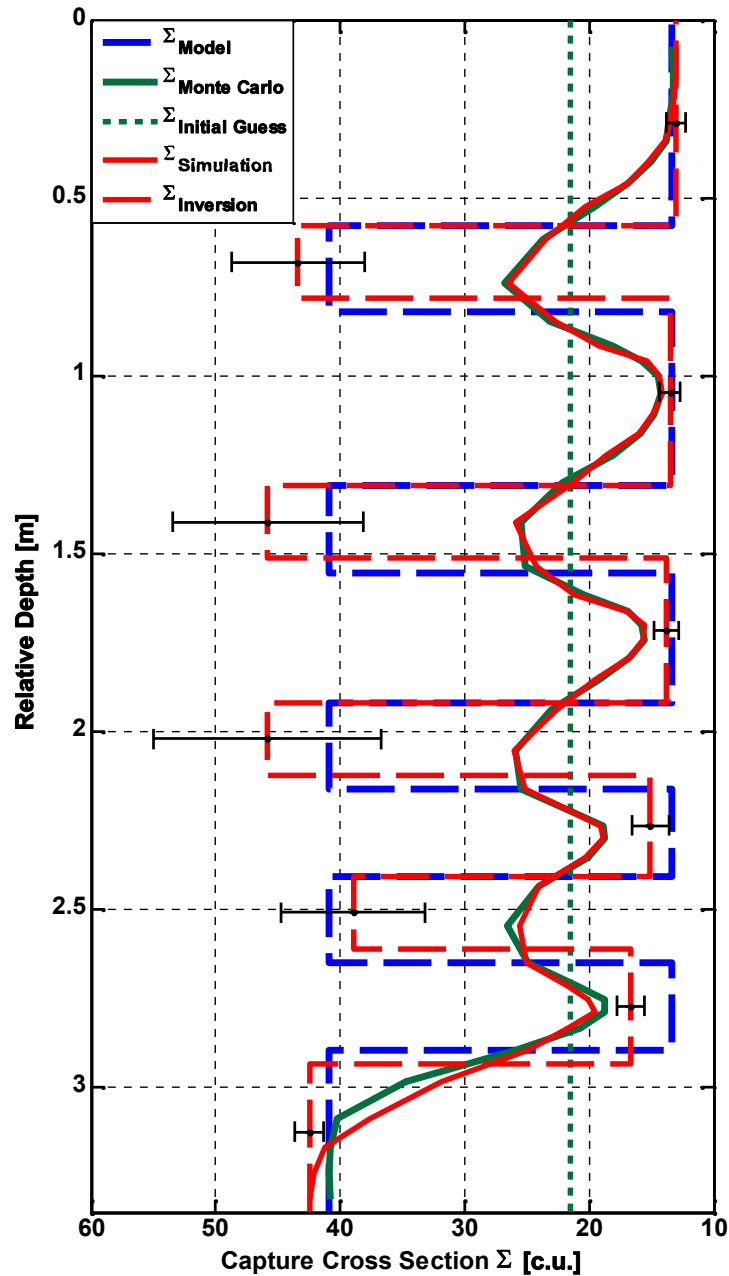


**Figure 7.4:** Impact of bed-boundary perturbation on the estimated layer-by-layer  $\Sigma$  values (dashed red line) for Synthetic Case No. 4. The true model is displayed with a dashed blue line. Numerically and measured  $\Sigma$  logs are indicated with solid red and green lines, respectively. The inversion was initialized with a parsimonious guess based on the average value of the measured log (dashed green line). Black error bars describe the 95% confidence interval.

## 7.4 FIELD EXAMPLES

### 7.4.1 Field Case No. 1

This field case is an open-hole test pit that includes 9.1 m of eleven different natural rock formations, comprising successive beds of sandstone, limestone, and dolomite. All formations are saturated with 35-kppm salt water. Low formation water salinity and absence of shale give rise to low values of  $\Sigma$ , spanning the range between 10 and 19 c.u. **Table 7.6** summarizes the corresponding properties of both formation water and borehole fluid, while **Table 7.7** describes the associated lithology, porosity, and bed thickness.

The right-hand panel of **Figure 7.4** shows results obtained for the numerical simulation of PNC measurements for this layered formation. Neutron and density logs are also included in the left-hand track. Upon convergence of the iterative inversion algorithm, which is achieved in 5 iterations and 7 seconds of CPU time, numerically simulated and field measurements agree within less than 1 c.u. **Table 7.7** describes the inverted layer-by-layer  $\Sigma$  values together with the 95% confidence interval for a 2% perturbation of the measured log. As expected, uncertainty in the estimations of  $\Sigma$  for 30.5-cm layers nos. 2, 3, and 4 is higher than in other beds; this behavior is due to the relatively larger correlation of model parameters in thinner beds.

This example also illustrates the importance of ancillary borehole measurements for accurate bed-boundary selection. As already emphasized in Synthetic Case No. 4, incorrect model layering yields biased inverted formation properties. PNC logs may not

properly resolve intermediate- $\Sigma$  beds, such as layer no. 10, owing to limitations of vertical resolution, together with concurrent diffusion effects occurring from lower- $\Sigma$  layer no. 9 and higher- $\Sigma$  layer no. 11. By contrast, the density log does indicate presence of a high-density layer between lower-density layers nos. 9 and 11.

Even though this field example does not include either casing or high- $\Sigma$  shales, the inversion exercise validates the reliability of our method to simulate and interpret PNC measurements in the case of actual field data. Accurate knowledge of bed boundaries and bed thickness provided by the test pit’s service company facilitated the implementation of the algorithm, given the importance of bed-boundary selection. We note that inversion does not sharpen PNC logs across thick beds as the estimated  $\Sigma$  values already coincide with the measured log. However, inversion does improve the assessment of  $\Sigma$  values in the thin 30.5-cm beds, as shown in the cases of layers nos. 3 and 4 of the test-pit model.

Variable	Value	Units
Formation water capture cross section	34.3	c.u.
Borehole fluid capture cross section	34.3	c.u.
Borehole diameter	21.0	cm
Sampling rate	15.2	cm

**Table 7.6:** Summary of the borehole diameter and sampling rate, as well as the assumed formation water and borehole fluid properties for Field Case No. 1.

#	Lithology	$2H$ [cm]	$\phi$ [%]	$\Sigma_{est}$ [c.u.]	$\delta\Sigma_{95}$ [%]
1	Limestone	91.4	25	15.0	3.05
2	Marble	30.5	0	14.9	6.56
3	Sandstone	30.5	19	17.5	6.78
4	Dolomite	30.5	0	12.1	7.73
5	Limestone	92.4	17	13.5	3.02
6	Sandstone	88.9	19	18.3	2.34
7	Marble	91.4	0	12.1	3.30
8	Chalk	91.4	26	13.4	3.08
9	Dolomite	85.1	0	10.6	3.98
10	Sandstone	48.3	8	13.8	4.41
11	Granite	182.9	0	21.2	1.51

**Table 7.7:** Summary of the assumed lithology, bed thickness  $2H$ , porosity  $\phi$ , estimated capture cross section  $\Sigma_{est}$ , and corresponding 95% confidence interval  $\delta\Sigma_{95}$ , from top to bottom of the formation, for Field Case No. 1.

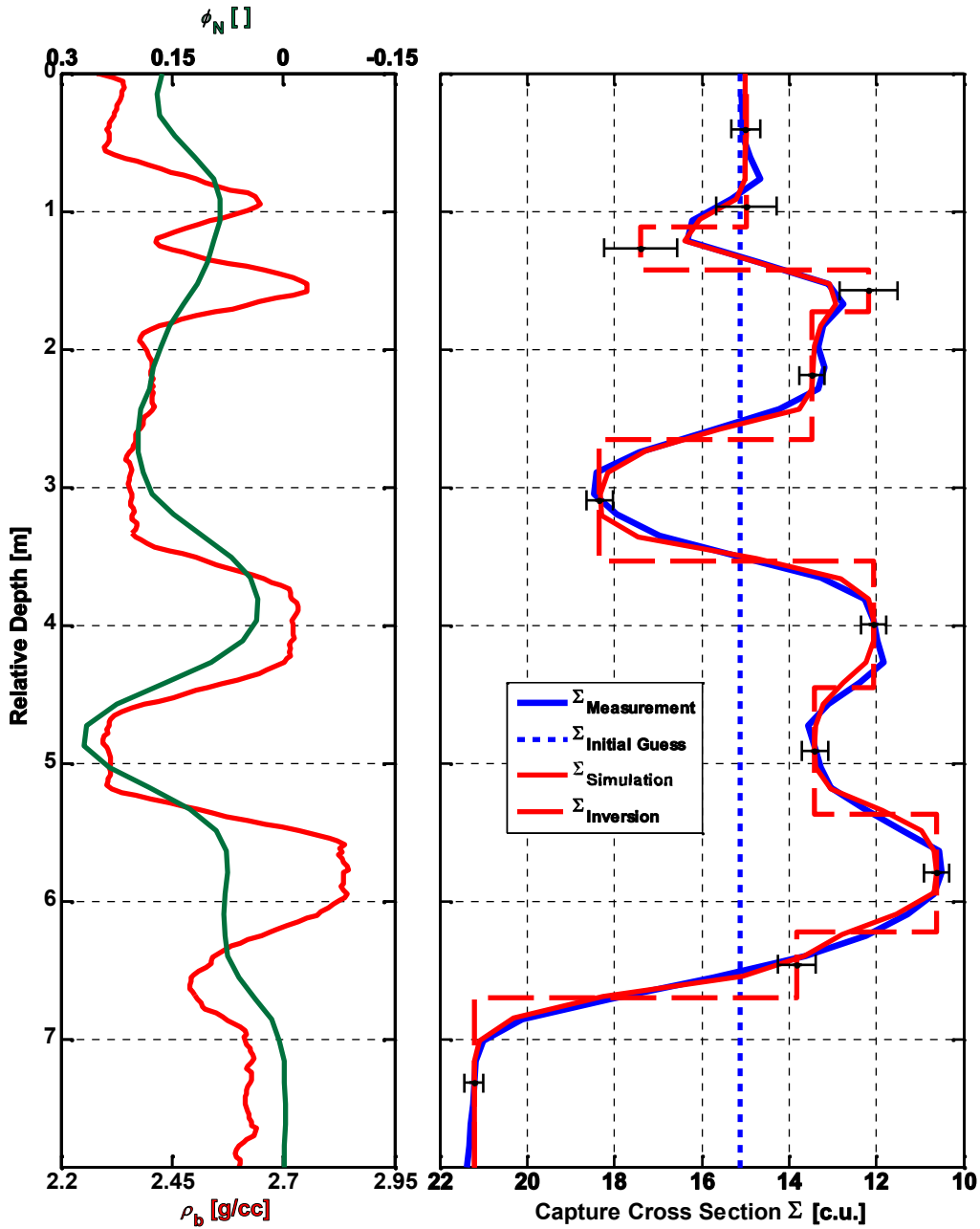


**Figure 7.5:** Comparison of numerically simulated (solid red line) and measured (solid blue line) PNC logs (right-hand track) for Field Case No. 1. The dashed blue line describes the initial guess, which is the average value of the measurements in this interval. Estimated layer-by-layer sigma values are indicated with dashed red lines, together with black error bars that quantify the 95% confidence interval. The left-hand track displays thermal neutron decay porosity (green) and density porosity (red) logs, respectively.



### 7.4.2 Field Case No. 2

This field case targets onshore, late Cretaceous to early Paleogene, steel-cased, tight-gas sand units in the Williams Fork formation (Piceance Basin, western Colorado). The formation consists of more than 600 m of lenticular, fluvial point-bar and crevasse-splay sandstone deposits, interbedded with associated overbank and floodplain siltstone and shale deposits (Pranter et al., 2008; Weijers et al., 2009). **Table 7.8** summarizes the formation properties for this field example. The relatively low values of porosity (6%) and salinity (19.5 kppm of NaCl equivalent) may prevent reliable interpretations of fluid saturation with the time-lapse equation for PNC logs. Also, unlike Field Case No.1, this example represents PNC measurements acquired in real field conditions, at several thousand meters underground, thereby amplifying potential noise and log depth shifts.

The right-hand panel of **Figure 7.6** shows the results obtained from the numerical simulation of the sigma log for 22 m of a shale-sand laminated formation. Tracks 1 through 3 show the open-hole gamma-ray, resistivity and neutron porosity logs, respectively. Bed boundaries were determined simultaneously from all the available open- and cased-hole logs. Five iterations in 30 seconds of CPU time were necessary to secure an acceptable match between simulated and measured logs within less than 1.3 c.u.

Even though inversion results obtained for this example are in agreement with the PNC log, they do not improve the  $\Sigma$  values already defined by the measurements. The reason for this behavior is two-fold: first, the average bed thickness is greater than the

vertical resolution of the tool; second,  $\Sigma$  spans the range from 10 to 25 c.u. only, whereby the corresponding shale-sand diffusion effects are not as significant as observed in the previous cases and, consequently, the measured log already provides an accurate description of the formation. This behavior results in low uncertainty in the determination of inverted formation properties (up to 4% for a perturbation of the log of 2%).

Variable	Value	Units
Porosity $\phi$	6	%
Formation water salt concentration $C_{wF}$	19.5	kppm
Standard deviation for $C_{wF}$	5.7	kppm
Formation water resistivity at 75°F	0.30	$\Omega.m$
Sampling rate	15.2	cm

**Table 7.8:** Summary of the average formation and fluid properties assumed for Field Case No. 2.

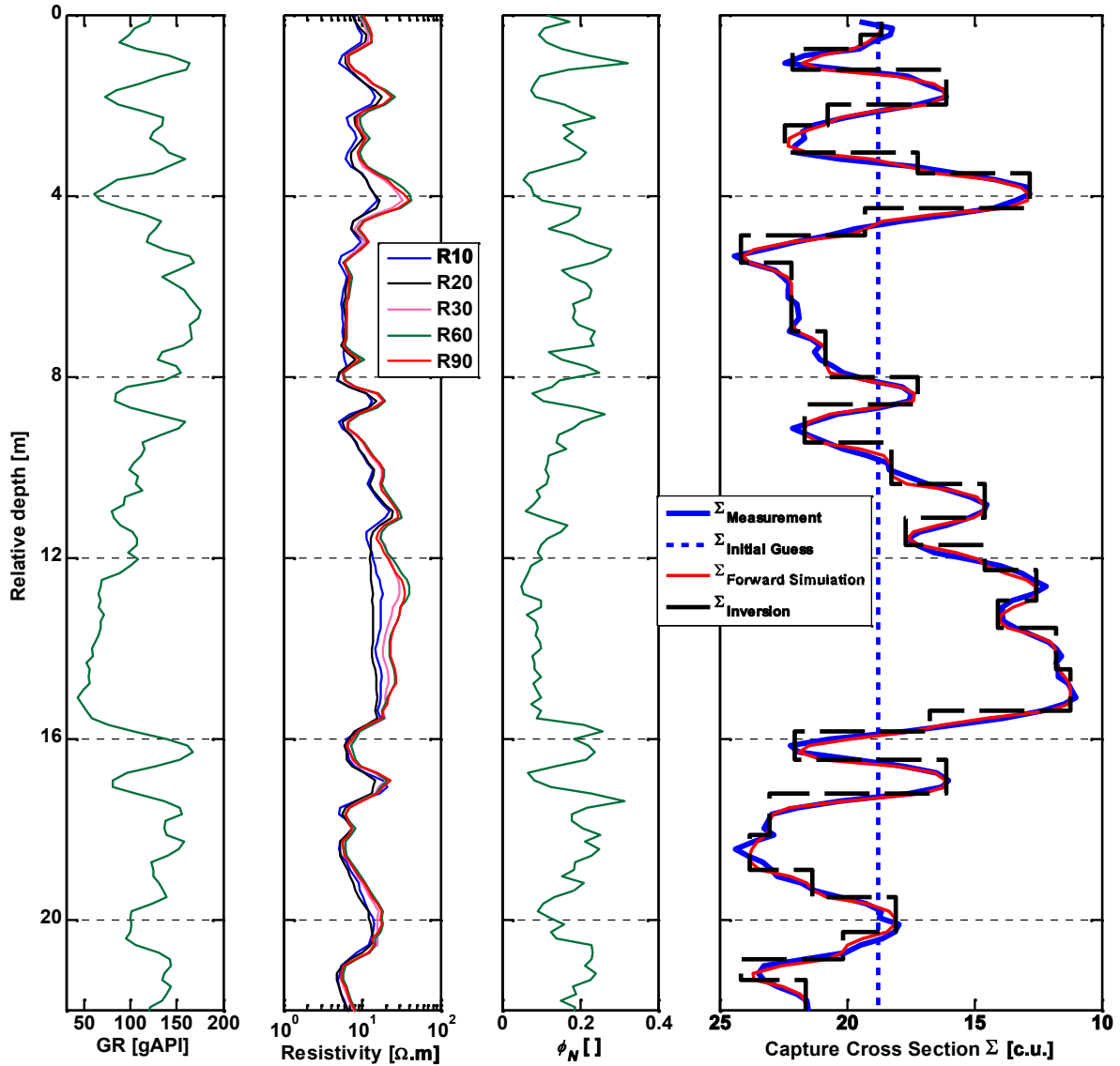


**Figure 7.6:** Comparison of numerically simulated (solid red line) and measured (solid blue line) PNC logs (track 4) for Field Case No. 2. The dashed blue line describes the initial guess, which is the average value of the measurements in this interval. Estimated layer-by-layer sigma values are indicated with dashed black lines. Track 1 displays the gamma-ray log; track 2 shows the array-induction resistivity logs; track 3 shows the neutron porosity log.

## Chapter 8: Conclusions and Recommendations

### 8.1 CONCLUSIONS

#### 8.1.1 Fast Numerical Simulation of PNC Logs

We developed a new numerical method to simulate PNC logs in seconds of CPU time that successfully substitutes time-prohibitive Monte Carlo methods. The agreement obtained against MCNP simulations indicates that the new simulation method properly captures the physics of PNC logging and diffusion effects that take place between dissimilar beds. Benchmarking examples included the cases of a thinly-bedded, turbiditic formation as well as a complex multi-layer formation, which encompassed most fluids and lithologies encountered in practice, with presence of borehole, casing, and cement.

The simulation algorithm initially solves the coupled neutron-and-photon transport equation with Monte Carlo methods to determine the base-case, late-time thermal-neutron flux sensitivity function included in our formulation of  $\Sigma$ . We invoked the distorted Born approximation to evaluate the ensuing expression for  $\Sigma$ , and validated the use of 1D neutron diffusion theory to approximate the spatial variations of the late-time, thermal-neutron FSFs in vertically heterogeneous formations. The correction procedure applied to measurements acquired across large contrasts of porosity and saturating fluids (i.e. with variable slowing-down lengths) resulted in maximum differences of 3 c.u. in the subsequent estimation of  $\Sigma$ . When applied to two benchmarking examples, the agreement

between numerically simulated logs and measurements was typically within 2-c.u. of error on average.

Although neutron measurements could be affected by substantial borehole environmental effects, our procedure does not explicitly account for them and does not require their calculation. Instead, we focus our efforts to the late-time formation signal, thereby implicitly assuming a high- $\Sigma$  borehole fluid configuration, which is typical of PNC logging.

Even though the results presented in this thesis were determined for a specific PNC-tool configuration, the base-case FSF can be readily adapted to any commercial data-acquisition configuration (source-detector spacing, tool diameter, etc.). Also, the simulation method could be readily extended to 2D and 3D geometries to account for deviated and horizontal wells, dipping beds, as well as invasion effects on measurements.

Our fast numerical method may be implemented in conjunction with inversion techniques to develop a quantitative petrophysical interpretation of  $\Sigma$  logs. Such a procedure could improve the interpretation of thinly-bedded formations and complex lithologies, to calculate layer-by-layer values of  $\Sigma$ . Finally, the method is fast enough to enable the quantitative integration of PNC logs with other open- and cased-hole logs.

### **8.1.2 Inversion in Thinly-Bedded Formations**

We invoked a previously introduced fast numerical simulation method of  $\Sigma$  logs to reconcile PNC measurements with layer-by-layer  $\Sigma$  values via inversion, especially in the cases of complex lithologies and thinly-bedded formations.

Except for bed boundaries, inversion examples required no a priori knowledge of formation properties to perform the estimation. The average value of the measurement log was a reliable initial guess to iteratively match the measured log within less than 1.3-c.u. Monte Carlo simulation methods would require several hours of CPU time to perform the calculations involved at every linear iteration of the nonlinear inversion procedure. For Synthetic Case No. 4, which includes 47 measurements points, this would represent more than 1800 hours of CPU time (assuming 4 hours per run and 10 iterations) By contrast, our method required no more than 10 seconds of CPU time to complete the inversion.

Inversion improves the estimation of layer-by-layer capture cross sections and reduces ambiguity in PNC logs across interbedded rock formations. In both synthetic examples, we systematically showed a significant contribution of inversion in the appraisal of thin layers, i.e. bed thickness between 24 and 45 cm. In these conditions, hydrocarbon-bearing sand layers were resolved by the inversion with maximum errors of 0.5 c.u., which is below the PNC-log reproducibility limit of 1.0 c.u. Quantitatively, we improved the definition of  $\Sigma$  logs by as much as 5.2 c.u. with respect to the original measurements. Similarly when applied to field data, our simulation and inversion method

reduced shoulder-bed effects and yielded enhanced estimates of layer-by-layer values of  $\Sigma$  by as much as 2 c.u. (Field Case No 1). For beds thicker than 45 cm, the log already provides reliable information that inversion does not improve, as observed with both Field Case No.2 as well as the lower section of Field Case No. 1.

Appraisal of the dependence on initial guess, measurement noise, and bed-boundary perturbations on inversion results indicated that PNC measurements are not severely nonunique. In terms of stability, as observed in Synthetic Case No. 4, the inversion is reliable in the presence of noisy measurements. However, the sensitivity analysis carried out for the same synthetic example showed that inversion results could be biased by erroneous detections of bed boundaries.

Accurate detection of bed boundaries is a critical step in our inversion method, especially in the interpretation of field data when there are no open-hole logs available to define bed boundaries which may not be resolved properly from smooth PNC logs. Synthetic and field examples indicated that inversion is a valuable method to assess the reliability of PNC logs: it was found that noisy or biased input logs (e.g. due to tool motion, tool sticking, depth mismatch, etc.) cannot be accurately reproduced with numerical simulations. In addition, we remark that numerical simulations will not reproduce field logs in cases where layers are not horizontal or when beds exhibit invasion effects.

## 8.2 RECOMMENDATIONS

The following is a list of recommendations for future research to extend the study considered in this thesis:

- i. The developed procedure can be extended to 2D and 3D geometries, including invasion<sup>4</sup>, dipping beds, deviated and horizontal wells. Radial and azimuthal directions should consequently be taken into account in the FSFs, and neutron diffusion theory should be applied with no further spatial approximations.
- ii. The study assumed that the importance of thermal neutrons was sufficient to accurately reproduce PNC measurements. The satisfactory results confirmed the relevance of this approximation. Nevertheless, in the case of radially changing properties (e.g. due to invasion, dipping beds, etc.), the impact of the formation on the transport of gamma rays may no longer be negligible. Future work could implement the coupling of thermal neutrons and photons.
- iii. Quantitative comparisons could be drawn between the present procedure and diffusion-based numerical simulators<sup>5</sup> to evaluate the benefits of using FSFs.
- iv. Commercial reservoir saturation monitoring programs go beyond the mere evaluation of  $\Sigma$ : they offer as well carbon-oxygen (C/O) ratio, spectroscopy, openhole resistivity, and resistivity behind casing. Further work could implement the joint<sup>6</sup> fast numerical simulation of these measurements, both for open- and case-hole conditions, for a variety of purposes:

---

<sup>4,5,6</sup> Relevant literature includes:

<sup>4</sup> Allen et al. (1965), Clavier et al. (1971a),

<sup>5</sup> Jennings and Weber (1995), Hamzah (1996).

<sup>6</sup> Ma et al. (2005), Okuku et al. (2008),



- a. Unlike PNC measurements, C/O logging<sup>7</sup> still brings reliable information in the cases of low or unknown formation water salinity. However, C/O use is limited by its depth of investigation.
- b. Further, spectroscopy could be extended beyond carbon and oxygen analysis, to obtain the complete lithology information<sup>8</sup>.
- c. Combining openhole resistivity measurements with cased-hole PNC measurements (e.g.  $R_t$ - $\Sigma$  crossplot<sup>9</sup>) could allow for detection of depleted zones as well as zones still affected by fresh mud filtrate invasion. Moreover, for mature reservoirs undergoing waterflooding and showing resistivity hysteresis, comparing resistivity- and  $\Sigma$ -derived saturations could allow for identification of flushed intervals<sup>10</sup>.
- d. Because  $\Sigma$  and C/O may suffer from borehole fluid invasion and reinvasion effects<sup>11</sup>, through openhole completions and existing perforations, openhole resistivity and resistivity behind casing may overcome such limitations by offering a greater depth of investigation. Nevertheless, the correct interpretation of resistivity measurements requires the detailed knowledge of formation water salinity and rock properties, which C/O,  $\Sigma$ , and spectroscopy logs may provide. Therefore, an integrated approach using nuclear and resistivity logs could lead to a thorough, self-consistent saturation evaluation.

---

<sup>7, 8, 9, 10, 11</sup> Relevant literature includes:

<sup>7</sup> Underwood et al. (1985), Zheng (2001),

<sup>8</sup> Herron and Herron (1996),

<sup>9</sup> Clavier et al. (1971a), Aguilera (1979),

<sup>10</sup> Gauthier et al. (2007),

<sup>11</sup> Kelder et al. (2006).

## Appendix A: FSF-Correction Procedure Based on 1D Diffusion Theory

### A.1 ASSUMPTIONS

Layered formations introduce model heterogeneities that cause perturbations on the FSFs. We calculate such perturbations under a set of assumptions. First, common subsurface materials exhibit a sufficiently low capture cross section compared to their total cross section; therefore, it is valid to assume that scattering is more likely to take place than absorption. Second, spatial variations of the neutron distribution are linear and we exclusively deal with isotropic scattering. Because the physics of PNC measurements involves mostly thermal neutrons, the diffusion equation (Stacey, 2007) may describe accurately the conservation of such mono-energetic neutrons under the conditions mentioned above, given by

$$-\nabla^2 \varphi(\mathbf{r}) + \frac{1}{L_d^2} \varphi(\mathbf{r}) = \frac{s}{D}, \quad (\text{A.1})$$

where  $\varphi(\mathbf{r})$  is thermal-neutron flux at position  $\mathbf{r}$ ,  $L_d$  is diffusion length,  $D$  is diffusion coefficient, and  $s$  is neutron source strength.

Also, we consider the PNC measurements to be acquired sufficiently late in time so that the contribution from the highly-absorbing borehole and casing become negligible. **Table A.1** describes the thermal decay times for typical formations, which are larger than those associated with both borehole fluid and casing, even for the case of high- shale lithology. This observation allows us to assume that diffusion takes place solely in the

vertical direction with no radial effect due to the borehole (we consider neither dipping beds nor mud-filtrate invasion in this study). Accordingly, the neutron conservation equation simplifies to the 1D diffusion equation, given by

$$-\frac{d^2}{dz^2}\varphi(z) + \frac{1}{L_d^2}\varphi(z) = \frac{s}{D}, \quad (\text{A.2})$$

where  $\varphi(z)$  is thermal-neutron flux at depth  $z$ .

Material	$\tau$ [ $\mu\text{s}$ ]	Description
Formation 1	690	Clean 15%-porosity sandstone, saturated with 100-kppm salt water ( $S_w = 0.3$ ) and methane ( $S_g = 0.7$ ).
Formation 2	291	Clean 20%-porosity limestone, saturated with 150-kppm salt water ( $S_w = 0.5$ ) and 0.82-g/cm <sup>3</sup> oil ( $S_o = 0.5$ ).
Formation 3	93.6	30%-porosity illite saturated with 250-kppm salt water.
Borehole fluid	37.0	250-kppm salt water.
Casing	21.0	Steel.

**Table A.1:** Thermal decay time  $\tau$  for various materials (calculated with SNUPAR).

## A.2 FORMULATION

We subsequently implement the principle of superposition for the linear differential equation (A.2), which enables us to decompose a complex multi-layer problem into elementary single-layer sub-problems. Such a procedure is equivalent to successively considering each layer as a source of thermal neutrons that diffuse into the surrounding layers. The initial distribution is given by the Monte Carlo-derived, late-time thermal-

neutron  $\text{FSF}_{\text{homog}}$ ; this function describes the flux of thermal neutrons in a homogeneous formation at late times, and already accounts for (a) the transport of high-energy neutrons, and (b) all residual borehole and radial effects.

Accordingly, for each sub-problem  $k$ , the diffusion-corrected FSF is calculated from

$$\begin{aligned}
 (\text{FSF}_{\text{corrected}})_k &= (\text{FSF}_{\text{homog}})_k \exp\left(-\frac{T_{\text{start}}}{\tau_k}\right) \\
 &\times \begin{cases} \sinh\left(\frac{H_k}{L_{dk}}\right) \exp\left(-\frac{z_k}{L_{dk}}\right), & z_k \in [H_k; \infty[ \\ 1 - \exp\left(-\frac{H_k}{L_{dk}}\right) \cosh\left(\frac{z_k}{L_{dk}}\right), & z_k \in [-H_k; H_k] \\ \sinh\left(\frac{H_k}{L_{dk}}\right) \exp\left(\frac{z_k}{L_{dk}}\right), & z_k \in ]-\infty; -H_k], \end{cases} \quad (\text{A.3})
 \end{aligned}$$

where  $(\text{FSF}_{\text{homog}})_k$  is Monte Carlo-computed, late-time thermal-neutron FSF for a homogeneous formation similar to layer  $k$ ,  $T_{\text{start}}$  is the delay necessary for borehole-effect cancellation,  $z_k$  is relative depth for sub-problem  $k$  (the reference origin is at the center of layer  $k$ ), and  $H_k$ ,  $L_{dk}$ ,  $\tau_k$  are half-thickness, diffusion length, and thermal decay time for layer  $k$ , respectively. We sum the individual  $(\text{FSF}_{\text{corrected}})_k$  for all the sub-problems  $k$  to obtain the FSF associated with the multi-layer problem, and normalize it in order to honor equation (4.2).

### A.3 RESULTS

**Figures A.1** and **A.2** show the thermal-neutron FSF calculated with this fast, approximate diffusion correction procedure (assuming knowledge of all formation properties), compared against the FSF computed directly from MCNP for a variety of layered formations. Values of  $\Sigma$  span the range from 10 to 50 c.u., with beds as thin as 24 cm. The correction procedure successfully reproduces the effects on the FSFs of multi-layer formations with similar slowing-down lengths  $L_s$  (Figure A.1), despite the multiple transitions across distinct materials. This results in less than 2-c.u. difference on the estimated  $\Sigma$ . The presence of the gas-bearing formations (represented in yellow) requires a specific treatment due to the lower hydrogen index, therefore the larger value of  $L_s$  compared to oil- and water-saturated formations. To that end, we apply the previously described corrections to another  $FSF_{\text{homog}}$ , previously calculated for the case of a homogeneous gas-bearing formation with similar value of  $L_s$ . Upon correction for presence of gas, the calculation procedure leads to approximate FSFs (Figure A.2), whose subsequent use gives rise up to a 3-c.u. difference on the estimated  $\Sigma$ .

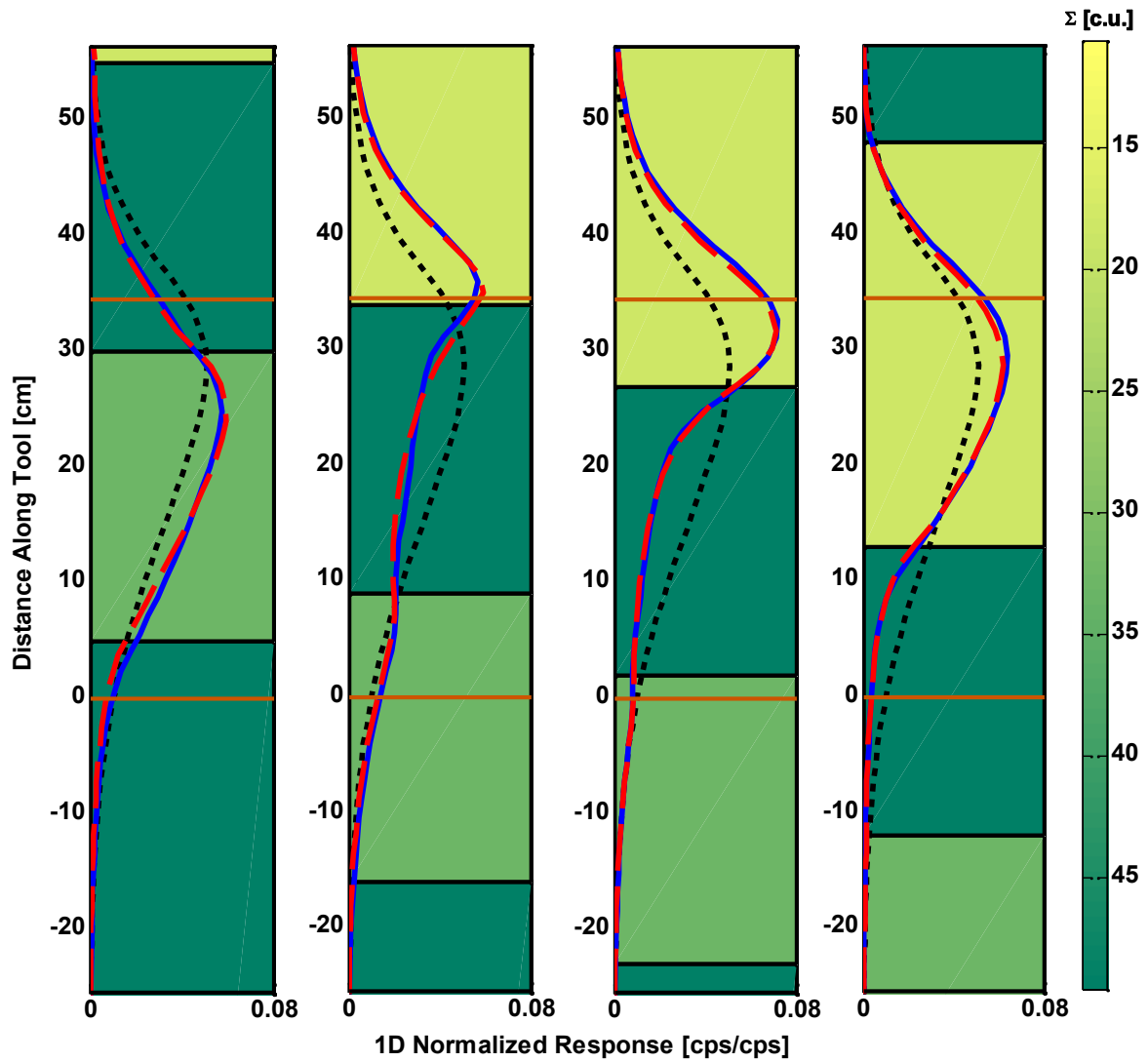


**Figure A.1:** Comparison of late-time, thermal-neutron FSFs simulated with the diffusion-approximation correction (dashed red line) and MCNP (solid blue line), for formations with similar slowing-down lengths (oil-, water-bearing sand, and shale formations). We initialized the correction procedure using the base-case FSF represented in dashed black line. Orange-colored lines at 0 and 35 cm describe the positions of source and detector, respectively.

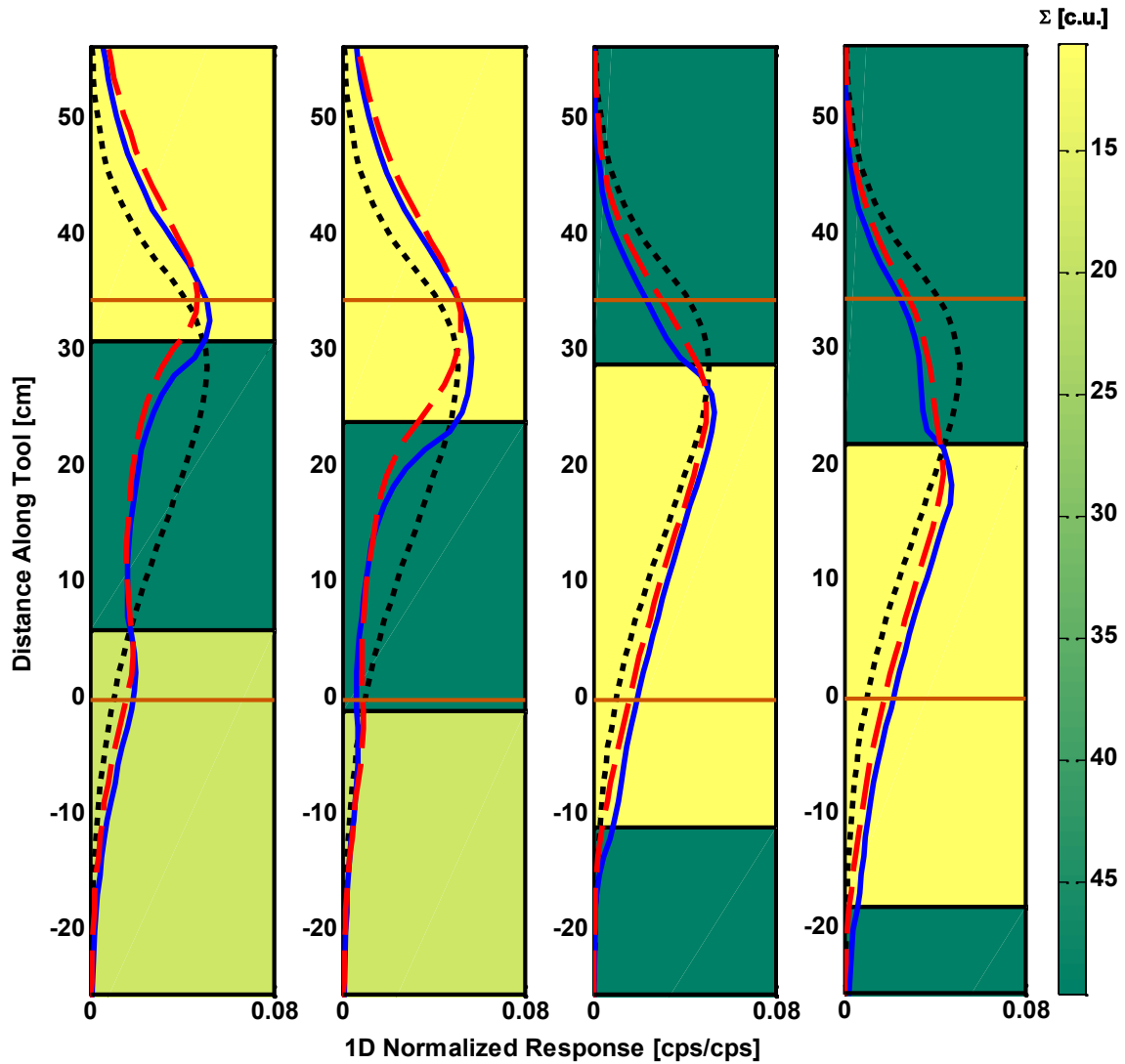


**Figure A.2:** Comparison of late-time, thermal-neutron FSFs simulated with the diffusion-approximation correction (dashed red line) and MCNP (solid blue line), for formations with different slowing-down lengths. We initialized the correction procedure using the regular base-case FSF (dashed black line) that is tailored to oil- and water-saturated formations (represented in light and dark green). For the gas-bearing formation (represented in yellow), we made use of a specific gas-formation FSF. Orange-colored lines at 0 and 35 cm describe the positions of source and detector, respectively.

## Nomenclature and Acronyms

### English

$A$	Amplitude of PNC signal, [cps/cps]
$C$	Volumetric concentration, [ ]
$C_w$	Salt concentration (NaCl equivalent) of connate water, [kppm]
$C(\mathbf{x})$	Quadratic cost function for inversion
$\mathbf{d}^0$	Vector of measured sigma log
$\mathbf{d}(\mathbf{x})$	Vector of numerically simulated sigma log
$\mathbf{e}(\mathbf{x})$	Vector of data residuals
$D$	Diffusion coefficient, [cm]
$H$	Half bed thickness, [cm]
$HI$	Hydrogen index, [ ]
$L_d$	Diffusion length, [cm]
$L_s$	Slowing-down length, [cm]
$M(t)$	Relative photon count, [cps/cps]
$\mathbf{r}$	Position vector
$s$	Neutron source strength, [particles/cm <sup>3</sup> ]
$S$	Saturation, [ ]
$t$	Time, [ $\mu$ s]
$\mathbf{x}$	Vector of layer capture cross sections
$z$	Vertical direction, [cm]



## Greek

$\lambda$	Regularization parameter for inversion
$\rho_b$	Bulk density, [g/cm <sup>3</sup> ]
$\Sigma$	Macroscopic capture cross section, [c.u.]
$\tau$	Thermal decay time, [ $\mu$ s]
$\phi$	Porosity, [%]
$\varphi$	Thermal-neutron flux, [particles/cm <sup>2</sup> ]

## Subscripts

BH	Borehole
<i>dif</i>	Expected measurement for the pure, infinite-extent formation in presence of borehole
<i>est</i>	Estimated
<i>exp</i>	Experimental
F	Formation
<i>g</i>	Gas
<i>h</i>	Hydrocarbons
homog	Homogeneous
<i>int</i>	Intrinsic
<i>k</i>	Layer <i>k</i>
LT	Late time
<i>ma</i>	Matrix
<i>o</i>	Oil
<i>s</i>	Non-Shale
<i>sh</i>	Shale
<i>sim</i>	Simulated
<i>w</i>	Water
0	Arbitrary
95	95% confidence interval

## Acronyms

cps	Count Per Second
c.u.	Capture Unit (1c.u. = $10^{-3}$ 1/cm)
FSF	Flux Sensitivity Function [ $1/\text{cm}^3\text{-eV}$ ]
kppm	Kilo Part Per Million
CPU	Computer Processing Unit
MCNP <sup>®</sup>	Monte Carlo N-Particle code
PNC	Pulsed Neutron Capture
SNUPAR	Schlumberger Nuclear Parameter Code
TDT <sup>®</sup>	Thermal Neutron Decay Time tool

## References

- Aguilera, R., 1979, A new approach for log analysis of the pulsed neutron and resistivity log combination: *Journal of Petroleum Technology*, **31**, no. 4, 415–418.
- Allen, L. S., W. R. Mills, and R. L. Caldwell, 1965, The effects of fluid invasion in pulsed neutron logging: *Geophysics*, **30**, 389–395.
- Aristodemou, E., C. Pain, C. de Oliveira, T. Goddard, and C. Harris, 2006, Energy group optimization for forward and inverse problems in nuclear engineering: application to downwell-logging problems: *Geophysical Prospecting*, **54**, 2, 99–120.
- Bartenhagen, K. J., J. C. Bradford, and D. Logan, 2001, Cased hole formation resistivity: Changing the way we find oil and gas: Society of Petroleum Engineers Permian Basin Oil and Gas Recovery Conference Proceedings, SPE 70042.
- Butler, J., 1987, A forward look at the calibration and correction of nuclear logging tools: test pits or transputers?: 28<sup>th</sup> Annual logging Symposium, Society of Petrophysicists and Well Log Analysts.
- Carmine, L., E. Aristodemou, C. Pain, A. Muggeridge, and C. de Oliveira, 2008, Inversion of time-dependent nuclear well-logging data using neural networks: *Geophysical Prospecting*, **56**, 1, 115–140.
- Clavier, C., W. Hoyle, and D. Meunier, 1971a, Quantitative interpretation of thermal neutron decay time logs: Part I. Fundamentals and techniques: *Journal of Petroleum Technology*, **23**, no. 6, 743–755.
- , 1971b, Quantitative interpretation of thermal neutron decay time logs: Part II. Interpretation example, interpretation accuracy, and time-lapse technique: *Journal of Petroleum Technology*, **23**, no. 6, 756–763.
- Cowan, P., and G. A. Wright, 1999, Investigations into improved methods of saturation determination using pulsed neutron capture tools: 40<sup>th</sup> Annual Logging Symposium, Society of Petrophysicists and Well Log Analysts, paper P.
- Dewan, J. T., C. W. Johnstone, L. A. Jacobson, W. B. Wall, and R. P. Alger, 1973, Thermal neutron decay logging using dual detection: *The Log Analyst*, **14**, no. 5, 13–26.
- Dunn, K., 1989, A diffusion model for pulsed neutron logging: *Geophysics*, **54**, 100–113.

- Ellis, D. V., and J. M. Chiaramonte, 2000, Interpreting neutron logs in horizontal wells: a forward modeling tutorial: *Petrophysics*, **41**, 1, 23–32.
- Flaum, C., M.- L. Mauborgne, and G. Weller, 2008, Method for extracting the value of thermal capture cross-section from pulsed neutron tool data by NMR-like inverse Laplace transform: 49<sup>th</sup> Annual Logging Symposium, Society of Petrophysicists and Well Log Analysts, paper K.
- Gauthier P. J., H. Hussain, J. Bowling, J. Edwards, and B. Herold, 2007, Determination of water-producing zones while underbalanced drilling horizontal wells – integration of sigma logs and real-time production data: Society of Petroleum Engineers Middle East Oil and Gas Conference Proceedings, SPE 105166.
- Guo, P., and J. Wang, 2009, Fast neutron log modeling in high angle and horizontal wells: 50<sup>th</sup> Annual logging Symposium, Society of Petrophysicists and Well Log Analysts, paper TT.
- Haley, R. A., 1995, Pulsed neutron capture log interpretation in laminated formations: A dual-exponential-decay model: *SPE Formation Evaluation*, **10**, no. 1, 20–25.
- Hamzah, S., 1996, Numerical simulation of pulsed neutron logging tools: M.S. thesis, New Mexico Institute of Mining and Technology.
- Hansen, P. C., 1994, Regularization tools: a Matlab package for analysis and solution of discrete ill-posed problems: *Numerical Algorithms*, **6**, no. 1, 1–35.
- Herron, S. L., and M. M. Herron, 1996, Quantitative lithology: an application for open and cased hole spectroscopy: 37<sup>th</sup> Annual Logging Symposium, Society of Petrophysicists and Well Log Analysts, paper E.
- Hopkinson, E. C., A. H. Youmans, and R. B. Jr. Johnson, 1974, Depth of investigation of the Neutron Lifetime Log: 15<sup>th</sup> Annual Logging Symposium, Society of Petrophysicists and Well Log Analysts, paper AA.
- Jennings, R. L., and G. A. Weber, 1995, Towards fast quantitative modelling of pulsed neutron logging tools: 36<sup>th</sup> Annual Logging Symposium, Society of Petrophysicists and Well Log Analysts, paper A.
- Kelder, O., A. A. Al-Hajari, and S. Crary, 2006, Borehole fluid reinvasion effects on C/O logs in openhole completion: Society of Petroleum Engineers Annual Technical Conference Proceedings, SPE 102543.
- Kimminau, S. J., and R. E. Plasek, 1992, The design of pulsed-neutron reservoir-monitoring programs: *SPE Formation Evaluation*, **7**, no. 1, 93–98.

- Locke, S., and R. Smith, 1975, Computed departure curves for the thermal neutron decay time log: 16<sup>th</sup> Annual Logging Symposium, Society of Petrophysicists and Well Log Analysts, paper S.
- Ma, S. M., A. A. Al-Hajari, G. Berberian, and R. Ramamoorthy, 2005, Cased-hole reservoir saturation monitoring in mixed-salinity environments – a new integrated approach: Society of Petroleum Engineers Middle East Oil and Gas Conference Proceedings, SPE 92426.
- Marquardt, D., 1963, An algorithm for least-squares estimation of nonlinear parameters: SIAM Journal of Applied Mathematics, **11**, no. 2, 431–441.
- McKeon, D. C., and H. D. Scott, 1989, SNUPAR – A nuclear parameter code for nuclear geophysics applications: IEEE Transactions on Nuclear Geoscience, **36**, no.1, 1215–1219.
- Mendoza, A., C. Torres-Verdín, W. E. Preeg, J. Rasmus, R. J. Radtke, and E. Stockhausen, 2009, Inversion of sector-based LWD density measurements acquired in laminated sequences penetrated by high-angle and horizontal wells: 50<sup>th</sup> Annual logging Symposium, Society of Petrophysicists and Well Log Analysts, paper N.
- Mendoza, A., C. Torres-Verdín, and W. E. Preeg, 2010, Linear iterative refinement method for the rapid simulation of borehole nuclear measurements, Part I – vertical wells: Geophysics, **75**, no. 1, pp. E9–E29.
- Mickael, M. W., 1999, A new algorithm for correcting neutron decay logs for borehole and diffusion effects: The Log Analyst, **40**, no. 6, 471–478.
- Mills, W.R., L. S. Allen, F. Selig, and R. L. Caldwell, 1965, Neutron and gamma-ray die-away in a heterogeneous system: Nuclear Applications, **1**, 312–321.
- Morris, F., C. Morris, and T. Quinlan, 2005, Applications of pulsed neutron capture logs in reservoir management: Society of Petroleum Engineers Western Regional Meeting Proceedings, SPE 93889.
- Murdoch, B. T., C. J. Hunter, R. R. Randall, and C. W. Towsley, 1990, Diffusion corrections to pulsed neutron capture logs: Methodology: 31<sup>st</sup> Annual Logging Symposium, Society of Petrophysicists and Well Log Analysts, paper Q.
- Nutt, R. L., and M. Watfa, 1989, Time-lapse saturation monitoring and its applications to time-lapse mapping: Society of Petroleum Engineers Middle East Oil Technical Conference and Exhibition, SPE 17975.
- Okuku, C., A. Zanoun, H. Ali, K. Nouredine, and N. Mokrani, 2008, Deriving matrix properties, fluid types and saturation from RST-CHFR combination in Siegenian

- reservoir of Bir Berkine field, Algeria: Society of Petroleum Engineers Annual Conference Proceedings, SPE 113489.
- Olesen, J.- R., M. Mahdavi, and D. K. Steinman, 1987, Dual-burst thermal decay time data processing and examples: 28<sup>th</sup> Annual Logging Symposium, Society of Petrophysicists and Well Log Analysts, paper U.
- Patchett, J. G., and R. Wiley, 1994, Inverse modeling using full nuclear response functions including invasion effects plus resistivity: 35<sup>th</sup> Annual logging Symposium, Society of Petrophysicists and Well Log Analysts, paper H.
- Peeters, M., D. W. Oliver, and G. A. Wright, 1994, Pulsed neutron tools applied to three-phase production-logging in horizontal wells: 35<sup>th</sup> Annual Logging Symposium, Society of Petrophysicists and Well Log Analysts, paper L.
- Plasek, R. E., R. A. Adolph, C. Stoller, D. J. Willis, E. E. Bordon, and M. G. Portal, 1995, Improved pulsed neutron capture logging with slim carbon-oxygen tools: Methodology: Society of Petroleum Engineers Annual Technical Conference Proceedings, SPE 30598.
- Pranter, M. J., M. F. Vargas, and T. L. David, 2008, Characterization and 3D reservoir modelling of fluvial sandstones of the Williams Fork Formation, Rulison Field, Piceance Basin, Colorado, USA: *Journal of Geophysics and Engineering*, **5**, 158–172.
- Preeg, W. E., and H. D. Scott, 1986, Computing thermal neutron decay time environmental effects using Monte Carlo techniques: *SPE Formation Evaluation*, **1**, no. 1, 35–42.
- Randall, R., E. C. Hopkinson, and A. H. Youmans, 1978, A study of the effects of diffusion on pulsed neutron capture logs: *Journal of Petroleum Technology*, **30**, 12, 1788–1794.
- Reedy, G. K., 1984, Accurate residual oil saturation measurement using a modified log-inject-log procedure: 25<sup>th</sup> Annual Logging Symposium, Society of Petrophysicists and Well Log Analysts, paper OOO.
- Richardson, J. E., R. E. Wyman, J. R. Jorden, and F. R. Mitchell, 1973, Methods for determining residual oil with pulsed neutron capture logs: *Journal of Petroleum Technology*, **25**, 5, 593–606.
- Serpas, C. J., P. A. Wichmann, W. H. Fertl, M. R. DeVries, and R. R. Randall, 1977, The dual detector Neutron Lifetime Log – theory and practical applications: 18<sup>th</sup> Annual Logging Symposium, Society of Petrophysicists and Well Log Analysts, paper CC.

- Sherman, H., and S. Locke, 1975, Depth of investigation of neutron and density sondes for 35-percent-porosity sand: 16<sup>th</sup> Annual Logging Symposium, Society of Petrophysicists and Well Log Analysts, paper Q.
- Simpson, G. A., and J. Y. Menke, 2010, Identifying low contrast – low resistivity pay zones with pulsed neutron capture logs in shaly sand Miocene formations of south Louisiana: 51<sup>st</sup> Annual Logging Symposium, Society of Petrophysicists and Well Log Analysts, paper O.
- Stacey, W.M., 2007, Nuclear reactor physics, Wiley-VCH.
- Steinman, D. K., R. A. Adolph, M. Mahdavi, and W. E. Preeg, 1988, Dual-burst thermal decay time logging principles: SPE Formation Evaluation, **3**, no. 2, 377–385.
- Stieber, S. J., 1970, Pulsed neutron capture log evaluation – Louisiana gulf coast: Society of Petroleum Engineers Annual Fall Meeting Proceedings, SPE 2961.
- Underwood, M. C., D. W. Mellor, and C. J. Dyos, 1985, A model of inelastic neutron scattering applied to the carbon/oxygen log: 26<sup>th</sup> Annual Logging Symposium, Society of Petrophysicists and Well Log Analysts, paper EEE.
- Wahl, J. S., W. B. Nelligan, A. H. Frentrop, C. W. Johnstone, and R. J. Schwartz, 1970, The Thermal Neutron Decay Time log: SPE Journal, **10**, no. 4, 365–379.
- Weijers, L., Y. Kama, J. Shemeta, and S. Cumella, 2009, Bigger is better – Hydraulic fracturing in the Williams Fork Formation in the Piceance Basin: Presented at the AAPG Annual Convention.
- Wiley, R., and J. G. Patchett, 1990, CNL neutron porosity modeling – a step forward: The Log Analyst, **31**, 3 133–149.
- X-5 Monte Carlo Team. MCNP, 2003, A general Monte Carlo N-particle transport code, v. 5, vol. II: user's guide: Los Alamos National Laboratory, <http://mcnp-green.lanl.gov/manual.html>, accessed 18 October 2009.
- Youmans, A. H., E. C. Hopkinson, R. A. Bergan, and H. F. Oshry, 1964, Neutron Lifetime, a new nuclear log: Journal of Petroleum Technology, **16**, no. 3, 319–328.
- Zheng, H., 2001, How the depth of investigation changes with spacing: a computer model for carbon/oxygen logging: Petrophysics, **42**, no. 1, 32–36.
- Zhou, T., J. R. Miles, C. R. Case, J. M. Chiaramonte, and D. V. Ellis, 2009, A second-order fast-forward model for a gamma-gamma density logging tool: Society of Petroleum Engineers Annual Technical Conference Proceedings, SPE 124193.

## **Vita**

Jordan Gilles Attia Mimoun was born in Échirolles, situated at the foot of the French Alps, on March 14, 1988, the second son of Gérard Mimoun and Monica Foglia. Upon graduation from high school in Échirolles (lycée Marie Curie) in 2004, Jordan studied math, physics and chemistry in preparatory school for two years in Grenoble (lycée Champollion). He joined École Centrale de Lille in northern France in 2006 where he received a Multidisciplinary Engineering degree. Between September 2008 and August 2010, Jordan was a research assistant with the Formation Evaluation Group in the Department of Petroleum and Geosystems Engineering at The University of Texas at Austin. In the summers of 2008 and 2009, he was an intern with Beicip-Franlab (IFP) in Paris and with the ExxonMobil Exploration Company in Houston, respectively. Upon completion of his Master's degree, Jordan will return to ExxonMobil's Formation Evaluation Core Group.

Permanent address:

3, rue Gabriel Didier  
38130 Échirolles  
France

Permanent email address:

[jmimoun@mail.utexas.edu](mailto:jmimoun@mail.utexas.edu)

This thesis was typed by the author.